Ising Nematic Quantum Critical Point in a Metal: A Monte Carlo Study

Yoni Schattner,[1] Samuel Lederer,[3] Steven A. Kivelson,[2] and Erez Berg[1]

[1]*Department of Condensed Matter Physics, The Weizmann Institute of Science, Rehovot, 76100, Israel*
[2]*Department of Physics, Stanford University, Stanford, California 94305, USA*
[3]*Department of Physics, Massachusetts Institute of Technology, Cambridge, Massachusetts 02139, USA*

(Received 26 November 2015; revised manuscript received 2 July 2016; published 23 August 2016)

The Ising nematic quantum critical point associated with the zero-temperature transition from a symmetric to a nematic metal is an exemplar of metallic quantum criticality. We carry out a minus-sign-free quantum Monte Carlo study of this quantum critical point for a two-dimensional lattice model with sizes up to 24×24 sites. For the parameters in this study, some (but not all) correlation functions exhibit scaling behavior over the accessible ranges of temperature, (imaginary) time, and distance, and the system remains nonsuperconducting down to the lowest accessible temperatures. The observed scaling behavior has remarkable similarities to recently measured properties of the Fe-based superconductors proximate to their putative nematic quantum critical point.

DOI: 10.1103/PhysRevX.6.031028

Subject Areas: Strongly Correlated Materials, Superconductivity

I. INTRODUCTION

A hallmark of strongly correlated electron systems is the competition of ground states with different kinds of order [1]. In this context, a central set of unsettled theoretical issues concerns the character of quantum critical points (QCPs) in metals [2–4]. Such metallic QCPs have been identified in several heavy fermion compounds [5]; evidence for quantum critical behavior has also been found in the ruthenate $Sr_3Ru_2O_7$ [6,7] and the cuprate and iron-based superconductors [8]. Quantum criticality is also often invoked as a possible explanation of the "strange" or "bad" metal behavior seen in a variety of such materials [13–20].

To date, there exists no satisfactory theory of metallic QCPs in $d = 2$ or 3 spatial dimensions although a number of field theoretic approaches have been attempted [21–39]. Among the unsettled issues are (a) the values of critical exponents and which properties can be expressed as scaling functions involving these exponents, (b) the extent to which metallic QCPs are generically preempted by superconducting [40–48] or other forms [43,49,50] of auxiliary order that gap out the Fermi surface, and (c) whether there exists a "non-Fermi liquid" metal in the quantum critical regime. Controlled theoretical methods, that can be used both to benchmark the field theories and for comparison with experiments, are greatly needed. Determinantal quantum Monte Carlo (DQMC) methods [51,52]—in particular, in cases where the fermion sign problem can be circumvented [53–55]—may serve this purpose. Such methods have been successfully applied in several problems in which critical bosonic fluctuations are coupled to fermions with a Dirac-like dispersion [56–59].

In this paper, we report a DQMC study of a two-dimensional sign-problem-free lattice model that exhibits an "Ising nematic" QCP in a metal at finite fermion density; in the nematic phase, the discrete lattice rotational symmetry is spontaneously broken from C_4 to C_2. This is a particularly relevant QCP given that nematic order [60–65] and nematic quantum critical fluctuations [11,66–70] have been observed in many of the materials mentioned above.

Our simulations are limited to finite system sizes—up to 24×24 lattice sites. Within our numerical accuracy, we find evidence for a continuous nematic quantum phase transition with critical behavior that differs significantly from that of a nematic QCP in an insulator. Specifically, in the disordered phase near the QCP, where the dimensionless quantum control parameter $h \geq h_c$, the thermodynamic (zero-frequency) nematic correlation function [defined in Eq. (4)] is consistent with the following functional description:

$$D(h, T, \mathbf{q}, i\omega_n = 0) \approx \left[\frac{A}{T^{\lambda} + b(h - h_c) + \kappa|\mathbf{q}|^2}\right]^{\gamma}, \quad (1)$$

where T is the temperature, $\mathbf{q}$ is the wave vector, ω_n is the Matsubara frequency, and A, b, and κ are positive dimensionful constants. We find that the exponents in this expression take values $\lambda = 1.0 \pm 0.1$ and $\gamma = 1.0 \pm 0.1$ (see Fig. 8). These values are in agreement with the predictions of Refs. [3,20,71,72] for the behavior of the thermodynamic susceptibility near criticality.

This implies that the uniform nematic susceptibility $\chi(h, T) \equiv D(h, T, \mathbf{0}, 0)$ has a Curie-Weiss form with an effective Weiss temperature that varies linearly with

Published by the American Physical Society under the terms of the Creative Commons Attribution 3.0 License. Further distribution of this work must maintain attribution to the author(s) and the published article's title, journal citation, and DOI.

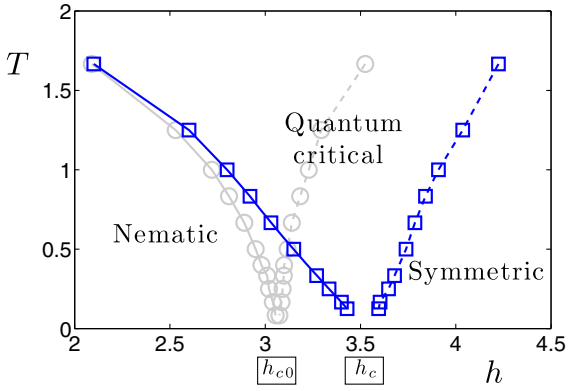

FIG. 1. Phase diagram of the model obtained by DQMC simulations, as a function of the transverse field h and temperature T. Here, the other parameters entering the Hamiltonian Eq. (3) are $V = t$, $\alpha = 0.5$, $\mu = -0.5t$. The solid line marks the transition temperature T_N between the nematic and the symmetric phases. The line extrapolates to the $T = 0$ QCP at h_c. The dashed line marks T_{cross}, where the nematic susceptibility reaches 50% of its magnitude at $h = h_c \approx 3.525$ at the same temperature. The gray lines show the corresponding temperatures for the case $\alpha = 0$ (where the fermions and pseudospins are decoupled). In this case, the QCP occurs at $h_{c0} \approx 3.06$.

$(h_c - h)$, as can be seen in Figs. 1 and 5. Equation (1) is consistent with the scaling relation $D(h, T, \mathbf{q}, 0) = \xi^{\gamma/\nu}\Phi(x, y)$, where $\xi \sim |h - h_c|^{-\nu}$, $x = T\xi^{\tilde{z}}$, $y = |\mathbf{q}|\xi$. Here, γ is the conventionally defined susceptibility exponent, the correlation length exponent $\nu \equiv \gamma/(2 - \eta)$, where η is the anomalous dimension of the nematic field, and we introduce an "apparent dynamical exponent" $\tilde{z} = (\nu\lambda)^{-1}$. The values of these exponents derived from our Monte Carlo data are given in Table I. We also include for comparison the exponents of the standard two-dimensional Ising QCP, which apply when the coupling to fermions is set to zero.

Despite the accuracy of the scaling analysis, it is important to test whether the observed behavior is characteristic of an asymptotic quantum critical scaling regime. To this end, we define a "quadrupolar" correlator Q in terms of fermion bilinears, which has the same symmetry as the nematic correlator D, and therefore should have the same asymptotic critical behavior. As can be seen in Figs. 9, 10, 11, and 14, Q does not obey a scaling law of the form of Eq. (1) over a comparable range of $(h, T, \mathbf{q})$ as does D. Sufficiently close to criticality, Q may be consistent with Eq. (1), but the dynamic range is relatively small and the error bars on the apparent exponents are substantial. It could be that corrections to scaling are smaller in D than in Q, or it could be that our data simply do not reflect asymptotic quantum critical scaling.

In the fermionic sector, we find results consistent with strongly renormalized Fermi-liquid, "marginal Fermi-liquid" [73], or weakly non-Fermi-liquid behavior down to our lowest temperatures ($T_{\min} \approx 0.02E_F$, where E_F is the Fermi energy). In particular, at the QCP, the effective quasiparticle weight, $Z_{\mathbf{k}_F}(T)$, defined in terms of the single-fermion Green function in Eq. (15), remains substantial. However, it monotonically decreases on cooling, with downward curvature. In a Fermi liquid, $Z_{\mathbf{k}_F}(T)$ would approach a positive limit as $T \to 0$, while in a weak non-Fermi liquid, it would vanish in proportion to a small power of T. Figure 2 shows maps of the low-energy spectral weight as a function of momentum in the disordered phase, at the QCP, and in the ordered phase. The existence [74] of "cold spots" along

TABLE I. Critical exponents for a 2D Ising QCP with $z = 1$ (classical 3D Ising), and scaling exponents from DQMC simulations near a metallic Ising nematic QCP. In the limit of vanishing coupling to the fermions, exponents from DQMC simulations are consistent with 3D classical Ising values. $\tilde{z}$ is the "apparent dynamical exponent" defined below Eq. (1).

Critical exponents	ν	γ	η	$\tilde{z}$
2D Ising QCP	0.63	1.24	0.04	1.0
2D *metallic* Ising nematic QCP	0.5 ± 0.1	1.0 ± 0.1	0.0 ± 0.3	2.0 ± 0.3

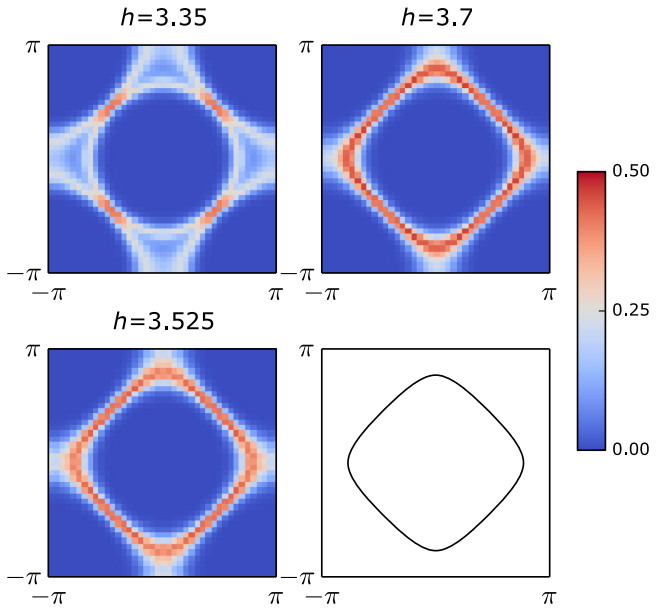

FIG. 2. Fermion Green's function $G(\mathbf{k}, \tau = \beta/2)$ as a function of momentum $\mathbf{k}$ across the Brillouin zone for three different values of the transverse field: $h = 3.35$ (in the nematic phase), $h = 3.525$ (near the QCP), and $h = 3.7$ (in the disordered phase). In the nematically ordered phase, the data are averaged over both orientations of the order parameter. $G(\mathbf{k}, \tau = \beta/2)$ is proportional to the integral of the spectral function $A(\mathbf{k}, \omega)$ over an energy window of width T [see Eq. (12)]. The temperature is $T = 1/8$, and the system size is $L = 20$. The data are taken from systems with either periodic or antiperiodic boundary conditions. The Fermi surfaces are seen as peaks in $G(\mathbf{k}, \tau = \beta/2)$. The lower right-hand panel shows the Fermi surface of the bare band structure.

the zone diagonals, where the quasiparticles are relatively weakly scattered, is apparent. Finally, no superconducting transition is found down to our lowest temperatures, although the superconducting susceptibility in the s-wave channel is peaked about $h \approx h_c$ (see Fig. 16).

The remainder of the paper is organized as follows: in Sec. II, we define the lattice Hamiltonian and describe its phase diagram; in Sec. III, we provide evidence for the statements above regarding thermodynamic nematic and quadrupolar correlations (Sec. III A), dynamical nematic and quadrupolar correlations (Sec. III B), superconductivity (Sec. III C), and single-fermion correlations (Sec. III D); finally, in Sec. IV, we discuss various caveats concerning the interpretation of our results and their bearing on both prior theoretical work and the interpretation of experiments.

II. MODEL AND PHASE DIAGRAM

Our model is illustrated in Fig. 3, and is defined on a two-dimensional square lattice. Every lattice site hosts a single (spinful) fermionic degree of freedom. Each link has a pseudospin-1/2 degree of freedom that couples to the fermion bond density. The system is described by the following Hamiltonian:

$$H = H_f + H_b + H_{\text{int}}, \tag{2}$$

where

$$\begin{aligned} H_f &= -t \sum_{\langle i,j\rangle,\sigma} c^\dagger_{i\sigma} c_{j\sigma} - \mu \sum_{i,\sigma} c^\dagger_{i\sigma} c_{i\sigma}, \\ H_b &= V \sum_{\langle\langle i,j\rangle;\langle k,l\rangle\rangle} \tau^z_{i,j} \tau^z_{k,l} - h \sum_{\langle i,j\rangle} \tau^x_{i,j}, \\ H_{\text{int}} &= \alpha t \sum_{\langle i,j\rangle,\sigma} \tau^z_{i,j} c^\dagger_{i\sigma} c_{j\sigma}. \end{aligned} \tag{3}$$

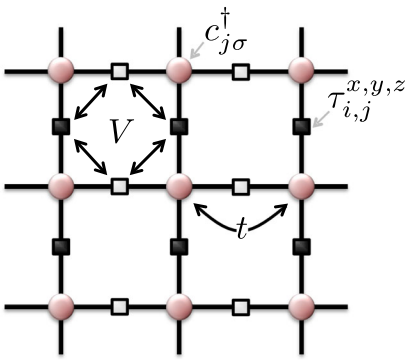

FIG. 3. Illustration of the lattice model Eq. (2). Spinful electrons reside on the sites, while the Ising pseudospins live on the bonds. The pseudospins interact with their neighbors antiferromagnetically, and are coupled to the fermion bond density.

Here, $c^\dagger_{j\sigma}$ creates a fermion on site j with spin $\sigma = \uparrow, \downarrow$, $\langle i, j\rangle$ denotes a pair of nearest-neighbor sites on the square lattice, t and μ are the hopping strength and chemical potential, respectively, $\tau^a_{i,j}$ $(a = x,\ y,\ z)$ denote Pauli matrices that act on the pseudospin that lives on the bond connecting the neighboring sites i and j, $V > 0$ is the nearest-neighbor Ising interaction between neighboring pseudospins (here, $\langle\langle i, j\rangle; \langle k, l\rangle\rangle$ denotes a pair of nearest-neighbor bonds), h is the strength of a transverse field that acts on the pseudospins, and α is the dimensionless coupling strength between the pseudospin and the fermion bond density.

The pseudospins are not related to the physical spins of the electrons; their ordering corresponds to a nematic transition. The model Eq. (2) should be viewed as an effective lattice model, designed to give a nematic QCP. Microscopically, the nematic degrees of freedom could represent (via Hubbard-Stratonovich transformation) interactions involving the same electrons that form the Fermi surface, or another, independent degree of freedom (such as a phonon mode that becomes soft at a structural transition). So long as the properties of the QCP are universal, the low-energy behavior does not depend on its microscopic origin.

For $\alpha = 0$, the system is composed of two decoupled sets of degrees of freedom: free fermions, and pseudospins governed by H_b, which has the form of a $d = 2$ transverse field Ising model. At zero temperature, the pseudospins undergo a second-order quantum phase transition from a paramagnet to an "antiferromagnet" that breaks 90° rotational symmetry at $h = h_{c0}$. This transition is in the three-dimensional classical Ising universality class. At $T = 0$, the pseudospin degrees of freedom are gapped in both the nematic and isotropic phases. At finite temperatures, a line of second-order classical $d = 2$ Ising transitions extends from the QCP in the h-T plane.

For nonzero α, the phase diagram is similar, but exhibits quantitative and qualitative modifications. Figure 1 shows the phase diagram, obtained by the DQMC simulations, for both $\alpha = 0$ and $\alpha \neq 0$. The $\alpha \neq 0$ transition between the nematic and isotropic phases remains second order, and extrapolates to a new QCP, shifted relative to h_{c0}. More striking is the change in the slope with which the phase boundary $T_N(h)$ approaches the QCP. For $\alpha = 0$, the slope diverges at low temperature, consistent with the expectation for the transverse field Ising transition, where $T_N \propto |h - h_{c0}|^{\nu z}$, with $\nu = 0.63$ and $z = 1$. In contrast, for $\alpha > 0$, we find that $T_N \propto (h_c - h)$. On the disordered side of the transition, we define a crossover line by identifying $h_{\text{cross}}(T)$ as the value of h at which the nematic susceptibility at fixed T has fallen to half of its value at $h = h_c$. $T_{\text{cross}}(h)$, the inverse of h_{cross}, also vanishes linearly with h upon approaching the QCP, although its slope is steeper than that of $T_N(h)$.

The linear behavior of $T_N(h)$ for small $h_c - h$ is also seen for other model parameters. In Fig. 4, we show the

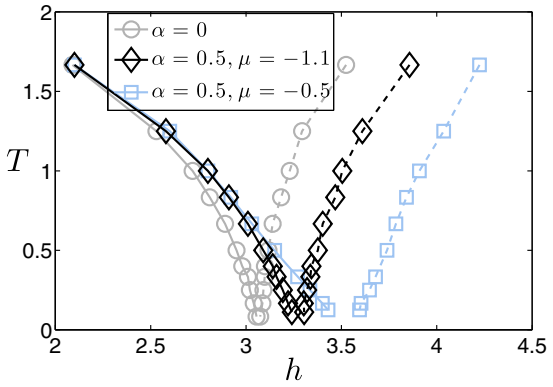

FIG. 4. The phase diagram for several sets of parameters. Gray circles represent the decoupled problem ($\alpha = 0$), while black diamonds and blue squares represent the coupled problem ($\alpha = 0.5$) at 0.6 and 0.8 fermions per site, respectively.

phase diagram for two values of the fermion density, controlled by the chemical potential μ. As the fermion density is reduced, both $h_c - h_{c0}$ and the range over which $T_N(h)$ is linear become smaller, indicating that the effect of the coupling between electrons near the Fermi surface and the nematic modes becomes weaker. The fact that $T_N(h)$ appears linear at low temperature for both values of fermion density is consistent with this being a *universal* property of the metallic QCP.

III. DQMC RESULTS AND ANALYSIS

We simulate the Hamiltonian Eq. (2) with system sizes between $L = 8$ and $L = 24$ and temperatures between $0.025t$ and $5t$. These simulations do not suffer from the minus sign problem: the fermion determinants obtained from integrating out the spin-up and spin-down fermions are identical and real, so the product is non-negative. Global updates of the pseudospin space-time configurations are introduced in order to overcome critical slowing down.

Some technical details related to the DQMC simulations are discussed in Appendix A. Here, we focus on the results and data analysis. Unless stated otherwise, the model parameters used in the simulations are $V = t$, $\alpha = 0.5$, $\mu = -0.5t$, $t = 1$.

A. Thermodynamic correlations

The two-point function for the nematic order parameter field is defined as

$$D(h, T, \mathbf{q}, i\omega_n) = \frac{1}{L^2}\sum_{i,j}\int_0^\beta d\tau e^{i\omega_n\tau - i\mathbf{q}\cdot\mathbf{r}_{ij}}\langle N_i(\tau)N_j(0)\rangle. \tag{4}$$

Here, $\mathbf{r}_{ij} = \mathbf{r}_i - \mathbf{r}_j$ and the nematic order parameter is defined as $N_i = \sum_j \eta_{ij}\tau^z_{ij}$, with $\eta_{ij} = 1/4$ for $\mathbf{r}_{ij} = \pm\hat{\mathbf{x}}$, $\eta_{ij} = -1/4$ for $\mathbf{r}_{ij} = \pm\hat{\mathbf{y}}$, and $\eta_{ij} = 0$ otherwise. The phase diagram discussed above is determined using the nematic susceptibility and standard finite-size scaling techniques described in Appendix B. We also define a quadrupolar order parameter, $\mathcal{N}_i = \sum_{j,\sigma}\eta_{ij}(c^\dagger_{i,\sigma}c_{j,\sigma} + c^\dagger_{i,\sigma}c_{i,\sigma})$ in terms of which the quadrupolar correlation function is

$$Q(h, T, \mathbf{q}, i\omega_n) = \frac{1}{L^2}\sum_{i,j}\int_0^\beta d\tau e^{i\omega_n\tau - i\mathbf{q}\cdot\mathbf{r}_{ij}}\langle \mathcal{N}_i(\tau)\mathcal{N}_j(0)\rangle. \tag{5}$$

Note that, while microscopically quite different, N and $\mathcal{N}$ have the same symmetries, and both develop anomalous expectation values in the nematic phase.

Figure 5 shows $\chi(h = h_c, T)$, which diverges upon cooling. Examining the data on a log-log plot [Fig. 5(b)], the susceptibility is seen to follow a power law, $\chi(h = h_c, T) = A/T^\lambda$ with $\lambda \approx 1$, over more than a decade of temperature between $0.1V < T \lesssim 2V$. The slope of $\log(\chi)$ versus $\log(T)$ is independent of the system size for $L \geq 12$.

To establish the scaling behavior of χ away from h_c, we plot the susceptibility for different temperatures and system sizes, as a function of $h - h_c$ [Fig. 6(a)]. For the system sizes displayed ($16 \leq L \leq 24$), χ is only weakly dependent on L. In Fig. 6(b), we plot $T^{\lambda\gamma}\chi(h, T)$ for $h > h_c$ as a function of $(h - h_c)/T^\lambda$, with $\lambda = 1.0$ and $\gamma = 1.0$. The different curves collapse onto each other, as expected for a scaling function.

Next, we examine the momentum dependence of the static correlator $D(h, T, \mathbf{q}, i\omega_n = 0)$ near the QCP. Figure 7 shows $D^{-1}(h, T, \mathbf{q}, i\omega_n = 0)$ as a function of $|\mathbf{q}|^2$ for various values of $h - h_c$ and T. For small momentum, the momentum dependence consists of an essentially isotropic term, approximately proportional to $|\mathbf{q}|^2$. Combined with the h and T dependences discussed above, we deduce that the static nematic correlator is well described by Eq. (1), with the aforementioned exponents, and with $A \approx 2.1$, $b \approx 2.9t$, $\kappa \approx 2.6t$, and the lattice spacing

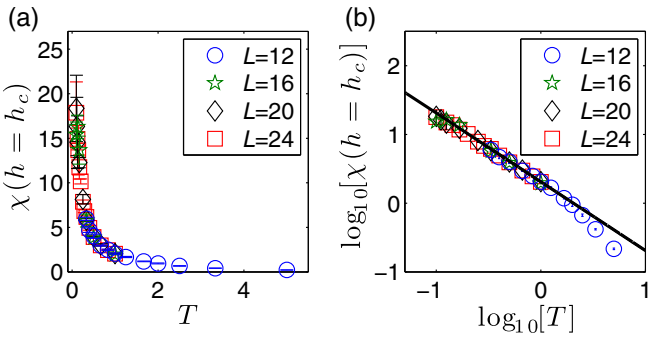

FIG. 5. Nematic susceptibility at the critical h, $\chi(h_c, T)$, as a function of temperature. Panel (a) shows the susceptibility on a linear scale. The same data are displayed on a log-log scale in (b). The black line is proportional to $1/T$.

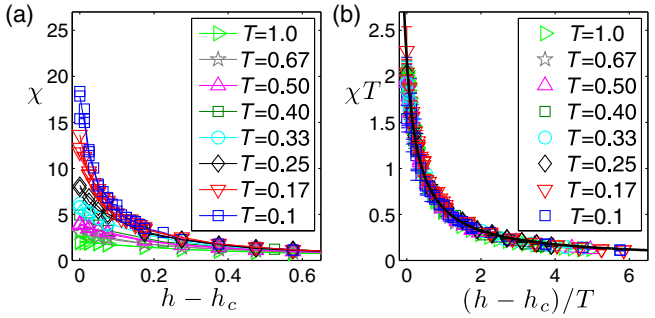

FIG. 6. (a) Nematic susceptibility $\chi(h,T)$ as a function of $h-h_c$ for system sizes $L=16$, 20, and 24 at various temperatures. (b) The same data, scaled appropriately for $\lambda=1$ and $\gamma=1$, collapse on a single curve. The black curve is the function $F(x)=2.1/(1+2.9x)$.

set to unity. This is explicitly demonstrated in Fig. 8. [In the figure, $\mathcal{A}(h,T,\mathbf{q},\omega_n)$ is the functional approximant to $D(h,T,\mathbf{q},\omega_n)$, defined in Eq. (6).]

In order to evaluate the consistency of the scaling form, Eq. (1), we also measure the quadrupolar correlator Q over a similar range of parameters as D. In Fig. 9, we compare the nematic and the quadrupolar susceptibilities at $h=h_c$ as a function of temperature. Like D, Q varies approximately linearly as a function of $1/T$, although there are large error bars at low temperatures. In Fig. 10, we show the h dependence of D^{-1} and Q^{-1} at various temperatures. In both cases, the h dependence is approximately linear for small $h-h_c$. However, the range of $h-h_c$ in which D^{-1} is linear is larger than the corresponding range of linearity of Q^{-1}, and the slope of D^{-1} at small $h-h_c$ is approximately T independent, while for Q^{-1} it is noticeably temperature dependent.

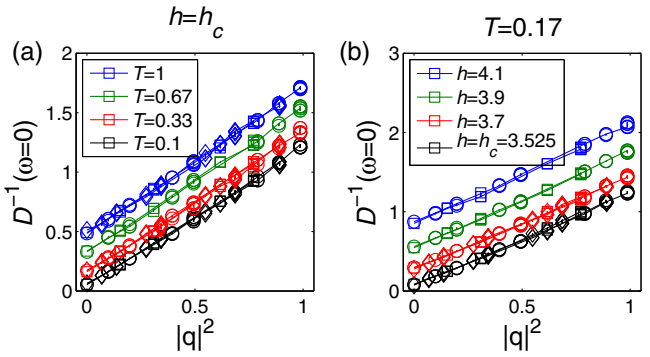

FIG. 7. Quadratic momentum dependence of the inverse nematic correlator at zero frequency. (a) D^{-1} versus $|\mathbf{q}|^2$ for all orientations of $\mathbf{q}$, at $h=h_c$ and various temperatures. (b) The same for fixed temperature $T=0.17t$ and a variety of values of the quantum tuning parameter h. In each case the momentum dependence remains quadratic. Momenta from multiple system sizes (represented by squares for $L=16$, circles for $L=20$, and diamonds for $L=24$) fall on the same curve, indicating that the properties shown are in the thermodynamic limit.

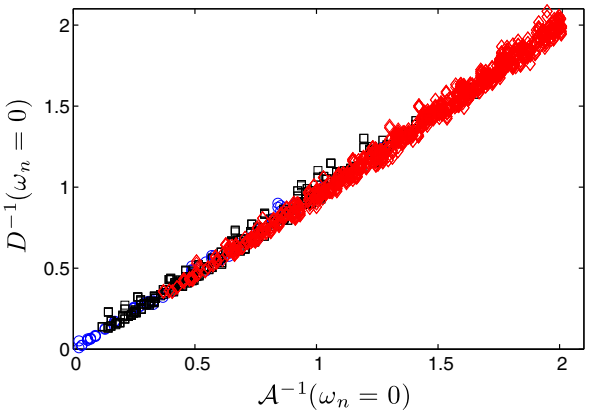

FIG. 8. Comparison between the thermodynamic ($\omega_n=0$) functional approximant $\mathcal{A}$, from Eq. (6), and the nematic correlator D. Data shown represent $L=16$, 20, and 24, $h=3.525$, 3.7, 3.9, and 4.1, and temperatures $T=1.0$, 0.67, 0.5, 0.33, 0.25, 0.17, 0.13, 0.1, 0.05, and 0.025. To exhibit the momentum dependence, we use blue circles for $\mathbf{q}=\mathbf{0}$ (71 data points), black squares for $|\mathbf{q}|=(2\pi/L)$ and $(2\pi/L)\sqrt{2}$ (568 data points), and red diamonds for all other $\mathbf{q}$ (1916 data points).

The momentum dependence of the two correlators is shown in Fig. 11. Both appear isotropic, depending only on $|\mathbf{q}|^2$. However, Q^{-1}, in contrast to D^{-1}, has noticeable downward curvature. D^{-1} depends on temperature through an essentially momentum-independent shift, while the temperature dependence of Q^{-1} is more complicated. For more details, see Appendix E.

B. Dynamic correlations

The dependence of D on Matsubara frequency, $\omega_n=2\pi Tn$, is shown in Fig. 12. At intermediate ω_n ($0.5t\lesssim\omega_n\lesssim 2t$) and for $\mathbf{q}\neq\mathbf{0}$, D^{-1} is an approximately linear function of $|\omega_n|$, with a slope that is independent of T, and also independent of both the direction and

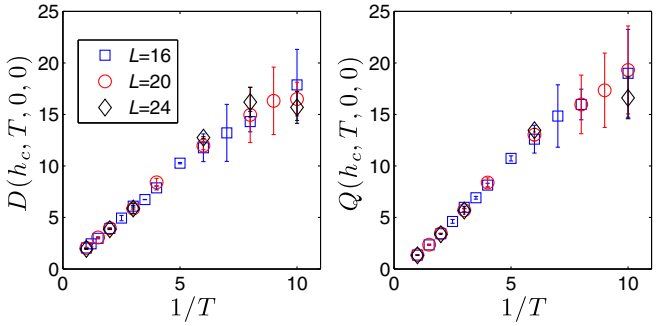

FIG. 9. Nematic and quadrupolar susceptibilities versus inverse temperature at $h=h_c$. Multiple system sizes are shown with squares for $L=16$, circles for $L=20$, and diamonds for $L=24$. The error bars reflect uncertainties due to finite system sizes, estimated from the differences between the measured susceptibilities of systems with different boundary conditions.

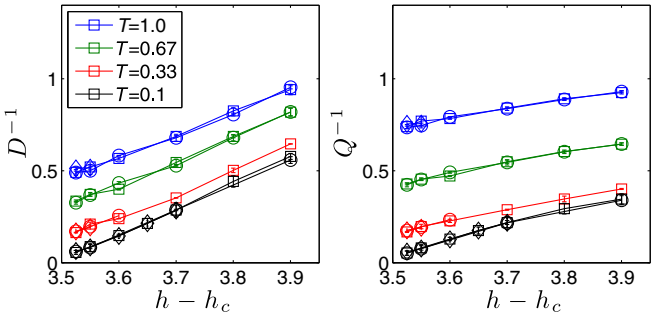

FIG. 10. Inverse nematic and quadrupolar susceptibilities versus $h - h_c$ at various temperatures. Multiple system sizes are shown with squares for $L = 16$, circles for $L = 20$, and diamonds for $L = 24$. The error bars reflect uncertainties due to finite system sizes, estimated from the differences between the measured susceptibilities of systems with different boundary conditions.

magnitude of $\mathbf{q}$. However, at the smallest nonzero momenta, a different frequency dependence is visible for $|\omega_n| < 0.5t$. This is emphasized in the inset of Fig. 12, where $D^{-1}(\mathbf{q}, i\omega_n = 0)$ has been subtracted. The frequency dependence at $\mathbf{q} = \mathbf{0}$ is different from the behavior seen for nonzero $\mathbf{q}$; for $\omega_n \lesssim t$, $D^{-1}(\mathbf{q} = 0, i\omega_n)$ appears to saturate to a frequency-independent value, followed by a sudden drop at $\omega_n = 0$. The frequency dependence of D^{-1} away from the critical point, shown in Fig. 23, is similar to the behavior of D^{-1} at criticality, apart from a constant positive shift [that corresponds to the fact that we are on the disordered side of the transition, and, hence, $D(\mathbf{q} = 0, i\omega = 0)$ remains finite in the thermodynamic limit].

The bulk of the data at small values of $h - h_c$, T, $\mathbf{q}$, and ω_n is well described by the simple "functional approximant" $D(h, T, \mathbf{q}, i\omega_n) \approx \mathcal{A}(h, T, \mathbf{q}, i\omega_n)$, where

$$\mathcal{A}(h, T, \mathbf{q}, i\omega_n) \equiv \frac{A}{T + b(h - h_c) + \kappa|\mathbf{q}|^2 + c|\omega_n|}. \quad (6)$$

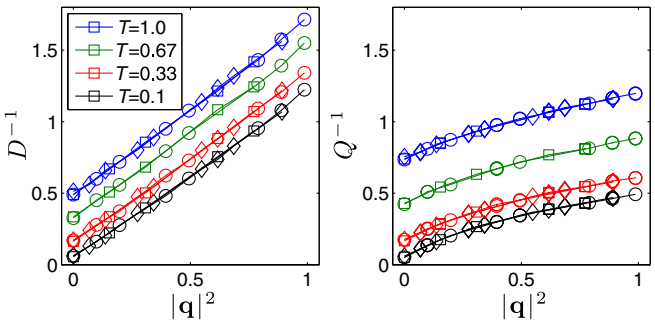

FIG. 11. Inverse nematic and quadrupolar correlators versus $|\mathbf{q}|^2$ for all orientations of $\mathbf{q}$ at $h = h_c$ and T from 0.1 to 1.0. Momenta from multiple system sizes (represented by squares for $L = 16$, circles for $L = 20$, and diamonds for $L = 24$) fall on the same curve, indicating that the properties shown are in the thermodynamic limit. Error bars are smaller than the symbol size.

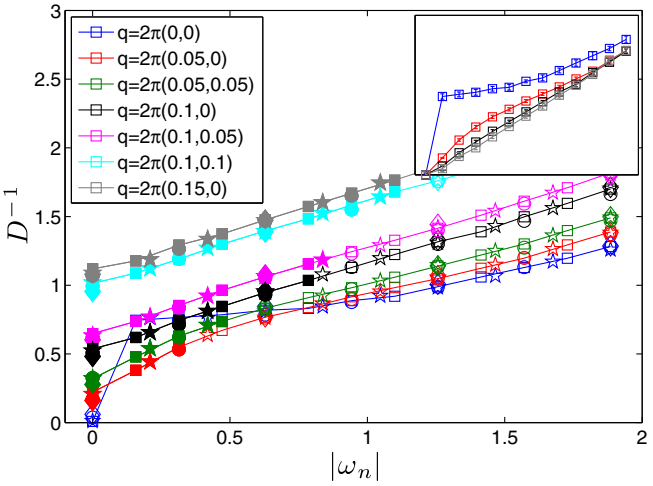

FIG. 12. Frequency dependence of the inverse nematic correlator at $h \approx h_c$ for a variety of small momenta $\mathbf{q}$ in an $L = 20$ system at temperatures $T = 0.025$, 0.033, 0.05, 0.1 (shown as squares, stars, circles, and diamonds, respectively). Different colors represent different values of $\mathbf{q}$, and filled symbols mark frequencies $|\omega_n| < v_F|\mathbf{q}|$, where v_F is the minimum value of the bare Fermi velocity. The frequency dependence is essentially linear except at the few smallest frequencies and momenta. The inset shows the subset of the data with $T = 0.025$ and momenta along the (10) direction shifted by their zero-frequency value, with the same scale as the main figure.

As shown in Fig. 8, this approximant is extremely accurate for all the data at $\omega_n = 0$. As can be seen from Fig. 24, it does an equally good job for the dynamical response for $\mathbf{q}$ not too small, but fails to describe the observed dynamics for the few lowest values of $|\mathbf{q}|$.

The equal time correlator gives complementary information about the dynamics, since it integrates over all frequencies. Moreover, "equal time" is the same in both real and imaginary time. Thus, in Fig. 13 we exhibit the inverse of the equal time correlator, $\tilde{D}(\tau = 0, \mathbf{r})$ for $h = h_c$ at $T = 0.1t$, as a function of distance for various values of L. Note that for the largest size system ($L = 24$), $\tilde{D}(0, \mathbf{r}) \sim 1/|\mathbf{r}|^2$, consistent with what one would get by Fourier transform of $\mathcal{A}$. $\tilde{D}$ is shown for all orientations of $\mathbf{r}$, so the narrow spread of points shows the high degree of isotropy exhibited by the data. Note also that for relatively small $|\mathbf{r}|$, the data are independent of L, at least for $L \geq 16$, but that at longer distances the data for the smaller systems deviate systematically from the $|\mathbf{r}|^{-2}$ behavior.

The frequency dependence of Q is shown in Fig. 14. It is clearly qualitatively different from the behavior of D in Fig. 12, and correspondingly cannot be approximated by any expression of the form in Eq. (6). The uniform quadrupolar density is nearly conserved, as is apparent from the very large values of $Q^{-1}(\mathbf{q} = \mathbf{0})$ at nonzero frequencies, shown in the inset of Fig. 14.

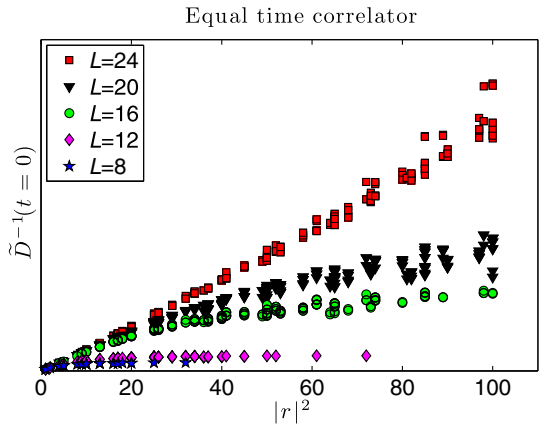

FIG. 13. The inverse of the equal time nematic correlator at $h = h_c$ and $T = 0.1$, plotted versus the square of the spatial separation $\mathbf{r}$ for various system sizes. The narrow spread in the data (which have not been chosen to lie along any high-symmetry direction) indicates an emergent isotropy of the correlations in this regime. The apparent $1/|\mathbf{r}|^2$ behavior in the thermodynamic limit is what one would get by Fourier transform of $\mathcal{A}$ from Eq. (6).

C. Superconductivity

We probe for superconducting correlations in the vicinity of the QCP by measuring the superfluid density and the superconducting susceptibility, as a function of h and T. The superfluid density is given by [75,76]

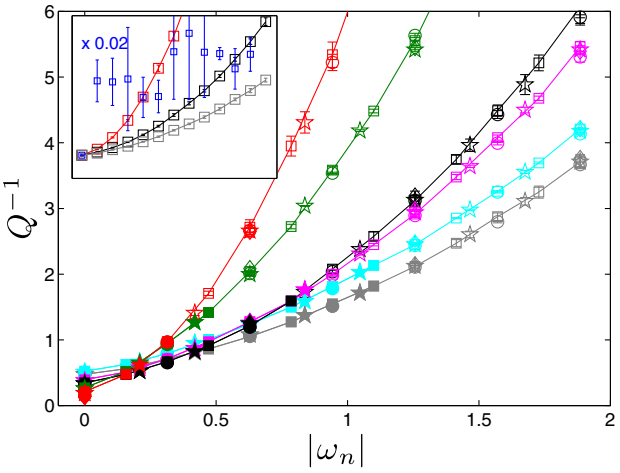

FIG. 14. Frequency dependence of the inverse quadrupolar correlator at $h \approx h_c$ for a variety of small momenta in an $L = 20$ system at temperatures $T = 0.025$, 0.033, 0.05, 0.1 (shown as squares, stars, circles, and diamonds, respectively). Different colors represent different values of $\mathbf{q}$, with the same color scale as in Fig. 12. Filled symbols mark frequencies $|\omega_n| < v_F|\mathbf{q}|$, where v_F is the minimum value of the bare Fermi velocity. The inset shows the subset of the data with $T = 0.025$ and momenta along the (10) direction shifted by their zero-frequency value, with the same scale as the main figure. The data for $\mathbf{q} = 0$ are scaled down by a factor of 0.02 to appear on the same scale.

$$\rho_s = \lim_{q_y \to 0} \lim_{L \to \infty} K_{xx}(q_x = 0, q_y), \tag{7}$$

where

$$K_{xx}(\mathbf{q}) \equiv \frac{1}{4}[\Lambda_{xx}(q_x \to 0, q_y = 0) - \Lambda_{xx}(\mathbf{q})], \tag{8}$$

and Λ_{xx} is the current-current correlator:

$$\Lambda_{xx}(\mathbf{q}) = \sum_i \int_0^\beta d\tau e^{-i\mathbf{q}\cdot\mathbf{r}_i} \langle j_x(\mathbf{r}_i, \tau) j_x(0,0)\rangle. \tag{9}$$

Here, the current density operator is given by $j_x(\mathbf{r}_i) = \sum_\sigma it(1 + \alpha\tau^z_{i,j}) c^\dagger_{i\sigma} c_{j\sigma} + \text{H.c.}$, where $\mathbf{r}_j = \mathbf{r}_i + \hat{x}$. $K_{xx}(\mathbf{q})$ describes the response of the system to a static orbital magnetic field $B(\mathbf{q})$:

$$j_x(\mathbf{q}) = -4K_{xx}(\mathbf{q}) A_x(\mathbf{q}), \tag{10}$$

where $A_x(\mathbf{q}) = iB(\mathbf{q})/q_y$ is the vector potential in an appropriate gauge.

Extrapolating K_{xx} to the thermodynamic limit is challenging due to the presence of strong finite-size effects associated with the Fermi surface. These finite-size effects are dramatically reduced by performing the computations in the presence of a weak uniform magnetic field [77]. We adopt this procedure, but make the field spin dependent, with the total flux through the system being 2π (-2π) for spin-up (spin-down). As shown in Ref. [53], such a procedure does not introduce a sign problem for the Monte Carlo technique. Moreover, in the limit of large system size, the magnetic field vanishes. (See Appendix A for the implementation of this effective magnetic field in the simulations.)

Figure 15 shows K_{xx} as a function of q_y, for different system sizes at temperature $T = 0.05$ and $h = h_c$. The data collapse onto a single curve that extrapolates to a value near zero in the limit $q \to 0$. The extrapolated value is clearly much below the universal value at the Berezinskii–Kosterlitz–Thouless (BKT) transition, $\rho_s^{\text{BKT}} = 2T/\pi$. This implies that at $h = h_c$ the system is not superconducting down to $T = 0.05t$. Similarly, the superfluid density for $h \neq h_c$ is found to be below ρ^{BKT} for all $T \geq 0.05t$. Note that, from Eq. (8), $\lim_{q_y \to 0} K_{xx}/q_y^2$ is the orbital susceptibility. From Fig. 15, we see that in our system this quantity is negative; hence, the orbital response is paramagnetic [78]. This indicates that there are no strong superconducting fluctuations (which would produce diamagnetism).

We also compute the superconducting susceptibilities in the s-wave (A_{1g}) and d-wave (B_{1g}) channels, as a function of h and T:

$$P_{s,d} = \int_0^\beta d\tau \sum_i \langle \Delta^\dagger_{s,d}(\mathbf{r}_i, \tau) \Delta_{s,d}(0,0)\rangle. \tag{11}$$

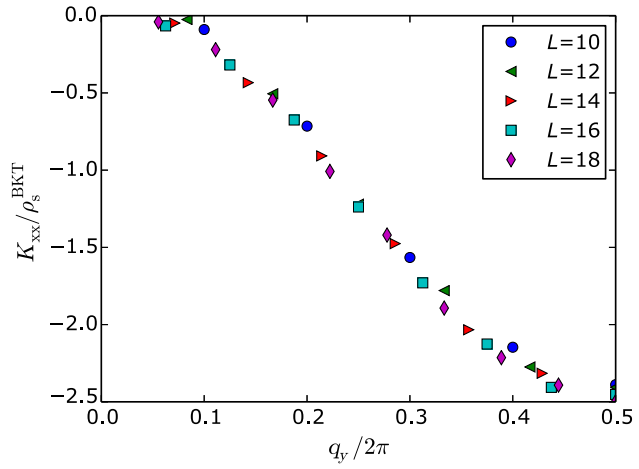

FIG. 15. $K_{xx}(q_x = 0, q_y)$ defined in Eq. (8) for $T = 0.05t$, $h = h_c$, and various values of system size, normalized by the universal value ρ_s^{BKT}. Momenta from different system sizes lie on the same curve, illustrating the thermodynamic limit. At small values of q_y, $K_{xx}(q_x = 0, q_y)$ lies well below ρ_s^{BKT}, indicating the system is not superconducting.

Here, $\Delta_s(\mathbf{r}_i) = c_{i\uparrow}c_{i\downarrow}$ and $\Delta_d(\mathbf{r}_i) = \sum_j \eta_{ij}(c_{i\uparrow}c_{j\downarrow} - c_{i\downarrow}c_{j\uparrow})$, where η_{ij} is defined below Eq. (4). The superconducting susceptibilities are displayed in Fig. 16. As expected for a nonsuperconducting state, both P_s and P_d saturate as a function of system size at fixed T and h [see Figs. 16(a) and 16(b)]. P_s has a maximum at $h \approx h_c$, while P_d is smaller and more or less independent of h.

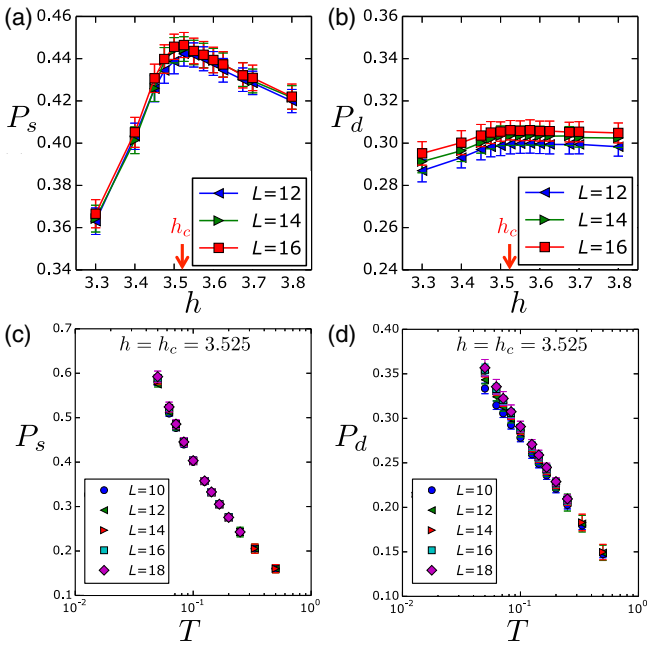

FIG. 16. (a),(b) Pairing susceptibility in the s-wave and d-wave channels, $P_{s,d}$ [Eq. (11)], as a function of h, at $T = 0.083$. Different system sizes are displayed. (c),(d) $P_{s,d}$ as a function of temperature at the QCP, $h = 3.525$.

The enhancement of P_s by nematic fluctuations is further reflected in its behavior as a function of temperature at a fixed h [Figs. 16(c) and 16(d)]. P_s rises more rapidly than logarithmically at low temperatures. In contrast for noninteracting electrons, $P \sim \log(T_0/T)$, a functional form consistent with the T dependence of P_d at low T. We interpret this as an indication that the s-wave susceptibility is enhanced by induced attractive interactions mediated by nematic fluctuations; the ground state for h near h_c is likely an s-wave superconductor, although with $T_c < 0.05t$.

D. Single-fermion correlations

Having found that the system is not superconducting down to the temperatures reached in this study, we examine the single-fermion Green function to glean information about the metallic state in the vicinity of the QCP. The metal is naturally characterized via the single-particle density of states $N(\omega)$, the Fermi velocity $\mathbf{v_F}$, and the quasiparticle weight $Z_{\mathbf{k_F}}$. However, extracting these quantities from DQMC simulations is not straightforward, since they generally require real-frequency information inaccessible without analytic continuation. In addition, $\mathbf{v_F}$ and $Z_{\mathbf{k_F}}$ are well defined only at zero temperature, while our simulations are at finite temperature. We partially resolve these difficulties by defining finite-temperature objects $\tilde{N}(T)$, $\mathbf{v_F}(T)$, and $Z_{\mathbf{k_F}}(T)$ which can be measured numerically, and whose zero-temperature limits are $N(\omega = 0)$, $\mathbf{v_F}$, and $Z_{\mathbf{k_F}}$, respectively. See Appendix D for the raw frequency dependence of the fermionic Green's function and self-energy.

Real-frequency information can be extracted from our imaginary-time data using the identity [79]

$$G(\mathbf{k}, \tau > 0) = \int_{-\infty}^{\infty} d\omega \frac{e^{-\omega(\tau-\beta/2)}}{2\cosh(\beta\omega/2)} A(\mathbf{k}, \omega), \tag{12}$$

where $A(\mathbf{k}, \omega)$ is the fermion spectral function. $G(\mathbf{k}, \beta/2)$ is evidently equal to the spectral function integrated over a range of energies $\sim T$. We, therefore, define

$$\tilde{N}(T) \equiv \frac{1}{T}\int \frac{d^2k}{(2\pi)^2} G(\mathbf{k}, \tau = \beta/2) = \int_{-\infty}^{\infty} \frac{d\omega}{2T\cosh(\beta\omega/2)} N(\omega), \tag{13}$$

$$\mathbf{v_F}(T) \equiv \frac{\partial^2}{\partial \mathbf{k}\partial\tau} \log\left[G(\mathbf{k}, \tau)\right]|_{\mathbf{k}=\mathbf{k_F}, \tau=\beta/2}, \tag{14}$$

$$Z_{\mathbf{k_F}}(T) \equiv 2G(\mathbf{k_F}, \tau = \beta/2). \tag{15}$$

We explain in Appendix C how these quantities attain the desired zero-temperature limits. We also discuss in the Appendix the procedures used to estimate these quantities

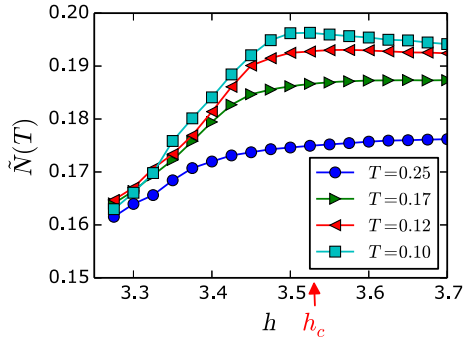

FIG. 17. $\tilde{N}(T)$, defined in Eq. (13), as a function of h for system size $L = 20$ at different temperatures. $\tilde{N}$ equals the density of states at the Fermi energy in the limit $T \to 0$.

in finite-size systems with discrete momentum and imaginary time.

Figure 17 shows $\tilde{N}(T)$ for an $L = 20$ system as a function of h, for different temperatures. $\tilde{N}(T)$ remains nonzero for all values of h, consistent with a finite density of states in the limit $T \to 0$. This indicates the absence of a substantial gap in the fermionic spectrum, even a gap with nodal points on the Fermi surface, down to $T = t/12$, corroborating the conclusion of Sec. III C that the system is not superconducting down to these temperatures. Moreover, the fact that $\tilde{N}(T)$ seems to neither vanish nor diverge at low temperature and $h = h_c$ has important implications for the nature of the metallic state of the QCP. Were the fermions to acquire a positive (negative) anomalous dimension η_F, the density of states would go to zero (diverge) at $T = 0$ [32,80]. We elaborate on this point in Sec. IV. Instead, the saturation of the density of states is consistent with a Fermi liquid, at least down to the temperature scales in our simulations. Note, as well, that the density of states appears to be depressed with increasing nematic order for $h < h_c$

The results for $Z_{\mathbf{k_F}}(\theta, T)$, where θ is the angle between $\mathbf{k_F}$ and the x axis, are shown in Fig. 18 for different values of $h \geq h_c$. At $\theta = 45°$, $Z_{\mathbf{k_F}}$ is close to unity at all temperatures. This can be understood as a consequence of the fact that at $\theta = 45°$ the coupling between fermions and the nematic critical modes vanishes by symmetry; hence, at these cold spots, the effects of scattering off the critical modes are minimal. $Z_{\mathbf{k_F}}$ decreases systematically as θ approaches 0°, and as h approaches h_c. $Z(k_F, \theta = 0, T)$ decreases with decreasing temperature with negative curvature. On the basis of the present data, it is difficult to say whether it extrapolates to a finite value in the $T \to 0$ limit [indicating a Fermi-liquid (FL) ground state] or vanishes with a small exponent, $Z \sim T^{a_Z}$, where $a_Z \approx 0.1$ (indicating a breakdown of FL behavior). It would be difficult to reconcile the data with a_Z larger than about 0.15.

Figure 19(a) shows the same data as a function of $h \geq h_c$ for $\theta = 0°$ and $\theta = 45°$, emphasizing the decrease in $Z_{\mathbf{k_F}}$ as

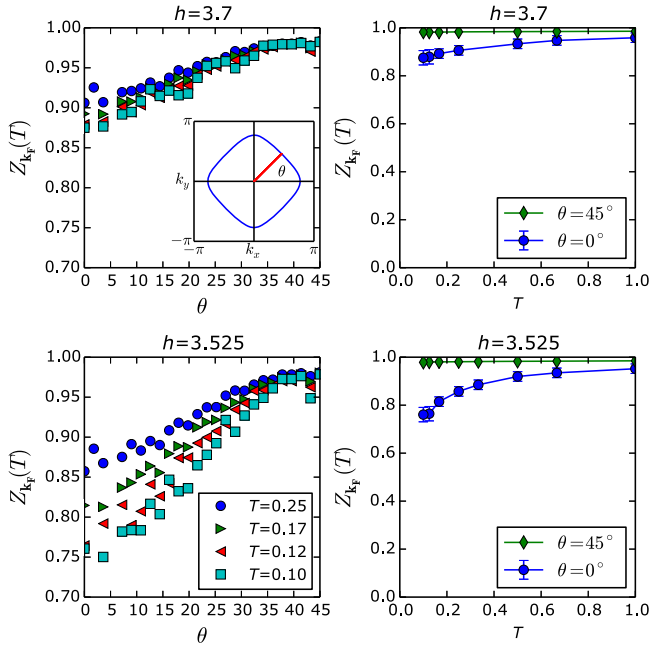

FIG. 18. Left-hand panels show $Z_{\mathbf{k_F}}$ [defined in Eq. (15)] as a function of angle θ along the Fermi surface, for different values of h. The QCP is at $h_c \approx 3.525$. Right-hand panels show the temperature dependence of $Z_{\mathbf{k_F}}(T)$ for high-symmetry directions of k_F. $Z_{\mathbf{k_F}}$ approaches the conventionally defined quasiparticle weight as $T \to 0$.

h approaches h_c. Measuring $Z_{\mathbf{k_F}}$ close to the QCP for $h < h_c$ (in the nematic phase) has proven difficult, since the two configurations of the order parameter correspond to two different Fermi surfaces with a small splitting between them. In Fig. 19(b), we show the renormalization of the Fermi velocity, $v_F/v_{F,0}$, where $v_{F,0}$ is the Fermi velocity for the noninteracting band structure ($\alpha = 0$). As with $Z_{\mathbf{k_F}}$, v_F is hardly renormalized at the cold spot $\theta = 45°$. In contrast, at $\theta = 0°$, v_F is strongly reduced from its

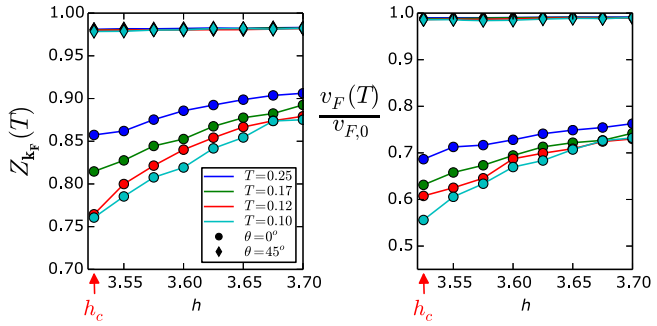

FIG. 19. (a) $Z_{\mathbf{k_F}}$ as a function of h for different temperatures. Circles (diamonds) correspond to $\theta = 45°$ ($\theta = 0°$) (where θ is defined in the inset of Fig. 18). (b) The Fermi velocity renormalization $v_F/v_{F,0}$ [where v_F is defined in Eq. (14) and $v_{F,0}$ is the noninteracting Fermi velocity] as a function of h for $\theta = 0°$, 45°.

noninteracting value, and the velocity renormalization increases as h approaches h_c. However, down to $T = 0.1t$, there is no obvious indication that v_F vanishes (i.e., the effective mass diverges) as $T \to 0$, even at $h = h_c$.

Over the temperature range we explore in this study, the single-fermion Green function is consistent with a renormalized Fermi liquid, with an angle- and h-dependent quasiparticle weight and velocity. However, the expected differences between a Fermi liquid and a marginal Fermi liquid or a weak (small a_Z) non-Fermi liquid are subtle at nonzero T. We can rule out a non-Fermi liquid with a substantial value of a_Z and/or η_F, but not one with a_z and η_F sufficiently small.

IV. DISCUSSION

We view our results as a numerical experiment. For an explicit lattice Hamiltonian, we obtain detailed and extensive measurements of physical quantities. In the neighborhood of the quantum phase transition, we find an enhanced tendency to superconductivity, substantial scattering of the fermionic quasiparticles, and a clearly delineated quantum critical fan. Moreover, for a large range of parameters, a simple scaling form provides a good description of the thermodynamic nematic fluctuations. In laboratory experiments on solid-state systems, good scaling collapse over a similar dynamical range is often interpreted in terms of universal critical exponents. However, in our system, the fermion bilinear quadrupolar correlations are only consistent with the apparent scaling form of the nematic correlator over a narrow region as a function of $(T, h - h_c, \mathbf{q})$. This is reason to question whether the behavior we are seeing is characteristic of the asymptotic approach to a quantum critical point. It is possible that the success of the scaling analysis is fortuitous. Alternatively, the observed scaling may reflect an intermediate asymptotic regime, possibly associated with an unstable multicritical point. It is also possible that corrections to universal scaling behavior are simply smaller for D than for Q, in which case the scaling form of D might reflect the true critical behavior. At the very least, the observation of simple power laws invites a comparison with theories of metallic quantum criticality.

A. Comparison with theory

The theory of metallic QCPs, along with the closely related theory of metals coupled to fluctuating gauge fields [81–83], has traditionally been treated by integrating out the fermions to obtain an effective action for the bosonic modes that is highly nonlocal in both space and time. In this Hertz-Millis approach, a renormalization group (RG) analysis is then undertaken for the effective field theory so defined. While much can be learned from this program, there are at least two general causes for concern. (1) The analyticity of the β function, which is a core ingredient of RG, is typically ensured by the locality of the action. For a nonlocal action, all aspects of the analysis, especially the enumeration of potentially relevant interactions that can be generated under RG, need to be tested explicitly. (2) In many cases, including, in particular, the 2D nematic QCP [74,84], if one considers the back effect of the collective fluctuations on the fermions, one finds that Fermi-liquid theory is perturbatively unstable. The question then arises concerning the self-consistency of the effective action that is obtained by integrating out an assumed Fermi liquid.

Nonetheless, there is a general feeling that this approach is reliable in large enough spatial dimension [85] [86], and its main results are similar in structure to those of many subsequent studies. Accordingly, we briefly review the main features of the Hertz-Millis treatment of the Ising nematic QCP.

In this context, the quadratic part of the effective action for the nematic mode is of the form

$$D_0^{-1}(\mathbf{q}, \omega_n) = r + \kappa|\mathbf{q}|^2 + \alpha^2 Q_0(\mathbf{q}, \omega_n), \tag{16}$$

where r and κ are (renormalized) functions of T and h, and Q_0 is the suitably defined particle-hole response function (with the zero-frequency piece subtracted),

$$Q_0(\mathbf{q}, \omega_n) \equiv \int \frac{d\mathbf{k}}{(2\pi)^2} \frac{i\omega_n |g(\mathbf{k}, \mathbf{q})|^2 [f(\varepsilon_{\mathbf{k}+\mathbf{q}}) - f(\varepsilon_{\mathbf{k}})]}{[\varepsilon_{\mathbf{k}+\mathbf{q}} - \varepsilon_{\mathbf{k}}][i\omega_n + \varepsilon_{\mathbf{k}+\mathbf{q}} - \varepsilon_{\mathbf{k}}]}, \tag{17}$$

where $g(\mathbf{k}, \mathbf{q})$ is a dimensionless form factor of appropriate symmetry, whose form depends on microscopic details [e.g., $g(\mathbf{k}, \mathbf{q}) = \cos(k_x) - \cos(k_y)$]. The essential features of this expression relate to its asymptotic (IR) behavior in the limit $E_F \gg |\mathbf{v_F}(\hat{\mathbf{k}}_\mathbf{q}) \times \mathbf{q}| \gg |\omega_n|$,

$$Q_0(\mathbf{q}, \omega_n) \sim |g(\hat{\mathbf{k}}_\mathbf{q}, 0)|^2 \frac{|\omega_n|}{|\mathbf{v_F}(\hat{\mathbf{k}}_\mathbf{q}) \times \mathbf{q}|}, \tag{18}$$

where $\hat{\mathbf{k}}_\mathbf{q}$ is the point on the Fermi surface (assumed to be unique mod inversion) at which the Fermi velocity $\mathbf{v_F}(\hat{\mathbf{k}}_\mathbf{q})$ is perpendicular to $\mathbf{q}$. [The fact that the integral in Eq. (17) for given $\mathbf{q}$ is dominated by the neighborhood of this point on the Fermi surface is the essential observation motivating the "patch" theories of this problem.]

The Hertz-Millis approach implies that the dynamical exponent $z = 3$ at tree level. From this, a naive scaling analysis (neglecting the possibility of higher-order nonlocal interactions) concludes that, since $d + z = 5$ is well above the Ising upper critical dimension, mean-field exponents $\nu = 1/2$, $\gamma = 1$, and $\eta = 0$ apply, consistent with what we find (see Table I). Moreover, one would expect violations

of scaling (for instance, $\tilde{z} \neq z$ and $\lambda \neq 1/\nu z$). Indeed, in Refs. [3,20,71,72] it is shown that at criticality such an analysis leads to $r \sim T \log[E_F/T]$. As we do not have the dynamical range to detect a logarithm, this, too, is consistent with our results.

However, on the face of it, our results for the dynamical nematic response are inconsistent with a dynamical exponent $z = 3$ and with the sort of anisotropies one might expect from the patch construction. Moreover, the relative weakness of any deviations of the single-particle properties from Fermi-liquid behavior appears inconsistent with the Hertz-Millis predictions [89]. On the other hand, at the smallest momenta, deviations of D from the scaling form $\mathcal{A}$, Eq. (6), become apparent. This may indicate a crossover [90] from an intermediate $z \approx 2$ regime to a different behavior in the deep infrared [91].

The foregoing discussion of the relation between our data and Hertz-Millis theory can be applied to numerous subsequent attempts to bring the problem under theoretical control. Among the approaches employed by these studies, whose results have similar structure to those of Hertz-Millis, are large N_F methods (where N_F is the number of fermion flavors) [21,24,25], dimensional [38,93,94] and dynamical [22,23,34] regularization, and higher-dimensional bosonization [95,96]. The related problem of orbital loop current criticality in a metal has been argued [15,97] to lead to a critical bosonic correlator with $|\omega|$ frequency dependence (as seen in our results), but with an asymptotic absence of momentum dependence (not seen in our results) characteristic of "local quantum criticality" [98]. In the vicinity of $d = 3$, several varieties of intermediate asymptotics corresponding to different schemes of large N_F and N_B (the number of boson flavors) have also been explored [37,99], at least one of which has $z = 2$ upon naive extrapolation to $d = 2$. We believe our results motivate revisiting existing theories of nematic quantum criticality in metals. In particular, the isotropy of bosonic correlations we observe appears to be at odds with patch constructions.

Finally, there has been considerable theoretical interest in the issue of superconductivity in the neighborhood of a nematic quantum critical point. It has been argued [41–43,47] that superconductivity with a critical temperature of order 1 times microscopic scales should be expected near the nematic quantum critical point. Indeed, it has been suggested that the superconducting T_c at criticality may be so high that it preempts the quantum critical regime in which non-Fermi-liquid behavior would be expected. More modestly, in the small α limit, it has been shown [46] that nematic fluctuations do indeed mediate attractive pairing interactions, and that the resulting transition temperature grows singularly as the quantum critical point is approached either from the ordered or the disordered side. In agreement with this latter result, the superconducting susceptibilities we show in Fig. 16 do show a maximum at $h = h_c$. However, if T_c at criticality is a number of order 1 times the Fermi energy, that number is apparently sufficiently small that $T_c < E_F/70$ for our chosen parameters. At larger values of the boson-fermion coupling constant, preliminary results [92] show that the ground state is an s-wave superconductor whose T_c is maximal near the nematic QCP.

B. Relation to experiment

There is increasingly extensive evidence that electron nematic phases are common in highly correlated electronic fluids [100]. In particular, it has been suggested that a nematic QCP occurs near optimal doping in both the cuprates [101,102] and the Fe-based superconductors [103,104]. However, the experimental situation in all these cases is complicated, and in some cases controversial.

It is premature to attempt any sort of serious comparison between the present results and the experiments in these materials. However, the experimental case is clearest in certain Fe-based superconductors, so it is worth noting a few points of comparison. Most strikingly, elastoresistance [11,66], Raman scattering [67,70], and elastic constant [69] measurements show a large range of T and doping over which a large nematic susceptibility can be documented with a remarkably systematic Currie-Weiss T dependence $\chi \sim 1/[T - T^*(x)]$, where $T^*(x)$ appears to depend roughly linearly on "doping" concentration x and to pass through zero at a critical doping concentration x_c, which approximately coincides with the optimal doping for superconductivity. It is impossible not to be encouraged by the similarity between this experimental finding and our numerical results.

ACKNOWLEDGMENTS

We are grateful to D. Chowdhury, A. Chubukov, S. Hartnoll, R. Fernandes, E. Fradkin, A. Millis, S. Raghu, and S. Sachdev for illuminating discussions. E. B. and Y. S. were supported by the ISF under Grant No. 1291/12, by the US-Israel BSF, and by a Marie Curie CIG grant. S. A. K. was supported in part by NSF Grant No. DMR 1265593 at Stanford. S. L. was supported in part by DOE Grant No. DE-AC02-76SF00515, an ABB Fellowship at Stanford, and a Gordon and Betty Moore Post Doctoral Fellowship at MIT.

Y. S. and S. L contributed equally to this work.

Note added.—Recently, a new theoretical analysis of the finite T dynamics near a nematic metallic QCP [105] has found a possible route to understanding the observed behavior of D, and, in particular, for the apparent dynamical exponent $z = 2$.

APPENDIX A: TECHNICAL DETAILS OF THE DQMC SIMULATIONS

Discretizing imaginary time as $\beta = N\Delta\tau$, the grand partition function becomes

$$\Xi = \mathrm{Tr}_{\{\tau\}}\mathrm{Tr}_{\{c,c^\dagger\}}\prod_{n=1}^{N/2}(\hat{B}\,\hat{B}^\dagger) + O(\Delta\tau^2), \tag{A1}$$

where

$$\hat{B} = e^{-(\Delta\tau/2)H_h}e^{-\Delta\tau H_V}e^{-\Delta\tau H_\mu}\prod_{m=1}^{4}(e^{-\Delta\tau c^\dagger K^{(m)}c})e^{-(\Delta\tau/2)H_h}. \tag{A2}$$

Here, $c^\dagger = (c^\dagger_{1,\uparrow}, c^\dagger_{1,\downarrow}, c^\dagger_{2,\uparrow}, c^\dagger_{2,\downarrow}, \ldots)$ is a row vector of spin-1/2 fermionic creation operators for the spatial sites $1, 2, \ldots, L^2$, where L is the linear dimension. H_h, H_V, and H_μ are the terms in Eq. (3) proportional to h, V, and μ, respectively. We use a checkerboard decomposition to describe the kinetic energy matrices $K^{(m)}$, whose elements are $K^{(m)}_{i,j,\sigma,\sigma'} = -t^{(m)}_{i,j}(\sigma)(1-\alpha\tau^z_{i,j})\delta_{\sigma,\sigma'}$; i.e., $m = 1, 2, 3, 4$ enumerates the horizontal or vertical bonds originating from a site with an even or odd index. We allow $t_{i,j}$ to depend on spin in order to implement the spin-dependent magnetic field discussed below.

Plugging in unity operators in the τ_{ij} sector at every time slice and taking the trace over the fermions, we bring the partition function to a form that can be sampled using Monte Carlo techniques:

$$\Xi = \sum_{\{\tau_{i,j;n}=\pm1\}} e^{-S_\tau}\det\left(1 + e^{\beta\mu}\prod_{n=1}^{N/2}T_{2n-1}T^\dagger_{2n}\right) + O(\Delta\tau^2), \tag{A3}$$

where $T_n = \prod_{m=1}^{4}(e^{-\Delta\tau K^{(m)}_n})$ is a matrix that depends implicitly on the c numbers $\tau_{i,j;n} = \pm1$ through the relation $K^{(m)}_{i,j,\sigma,\sigma';n} = -t^{(m)}_{i,j}(\sigma)(1-\alpha\tau_{i,j;n})\delta_{\sigma,\sigma'}$, and the bosonic part of the action is given by

$$S_\tau = \frac{1}{2}\log\left[\tanh(\Delta\tau h)\right]\sum_{\langle i,j\rangle,n}\tau_{i,j;n}\tau_{i,j;n+1} + V\Delta\tau\sum_{\langle\langle i,j;k,l\rangle\rangle,n}\tau_{i,j;n}\tau_{k,l;n}. \tag{A4}$$

We use $\Delta\tau = 0.05$ in our simulations.

Monte Carlo sampling is most efficient when the determinant in Eq. (A3) is positive. Here, the absence of a sign problem is guaranteed by microscopic time-reversal symmetry. To see this, note that the matrices T_n are block diagonal in the spin sector, and so the total determinant is the product of the spin-up and spin-down determinants. If time reversal is preserved, i.e.,

$$t_{i,j}(\uparrow) = t^*_{i,j}(\downarrow), \tag{A5}$$

the product of the determinants is clearly positive.

It has long been known [77] that finite-size effects in fermionic systems, in particular at low temperatures, can be greatly improved by the application of a weak orbital magnetic field. On a finite-size system with periodic boundary conditions, the field must be such that an integer multiple of the flux quantum passes through the system, $\Phi = n\Phi_0$. In order to preserve time-reversal symmetry as required in Eq. (A5), in this work we apply the opposite field for both spin species, such that $\Phi_\uparrow = -\Phi_\downarrow = \Phi_0$. Such a field vanishes in the thermodynamic limit.

Although our simulations do not suffer from the sign problem, close to the quantum critical point our simulations do suffer from critical slowing down. To avert this, we find it helpful to include global Monte Carlo updates, in addition to local (Metropolis) ones. Our global updates consist of a slight modification to the Wolff algorithm [106]: Starting from a space-time configuration of pseudospins, a cluster of pseudospins is constructed using the usual Wolff algorithm, supposing our action is given by Eq. (A4), i.e., without taking into account the coupling to the fermions. Next, we propose flipping the pseudospins which belong to the cluster, and accept the move with a probability that is the ratio of the determinants in Eq. (A3) between the two configurations. It can easily be seen that such a move obeys detailed balance.

APPENDIX B: FINITE-SIZE SCALING ANALYSIS

The finite-temperature phase boundary $T_N(h)$ [or equivalently $h_N(T)$] can be computed by using *classical* finite-size scaling techniques for two-dimensional Ising transitions, characterized by susceptibility exponent $\gamma = 7/4$ and correlation length exponent $\nu = 1$. At a given temperature and for a given system size L, the most singular part of the thermodynamic susceptibility χ_s satisfies

$$\chi_s(h;L) = L^{\gamma/\nu}F[(h-h_N)L^{1/\nu}]; \tag{B1}$$

h_N can, therefore, be identified using a single-parameter data collapse, as illustrated in Fig. 20. At low temperatures, the region of parameter space corresponding to classical criticality narrows, so that larger system sizes are needed to reliably estimate h_N.

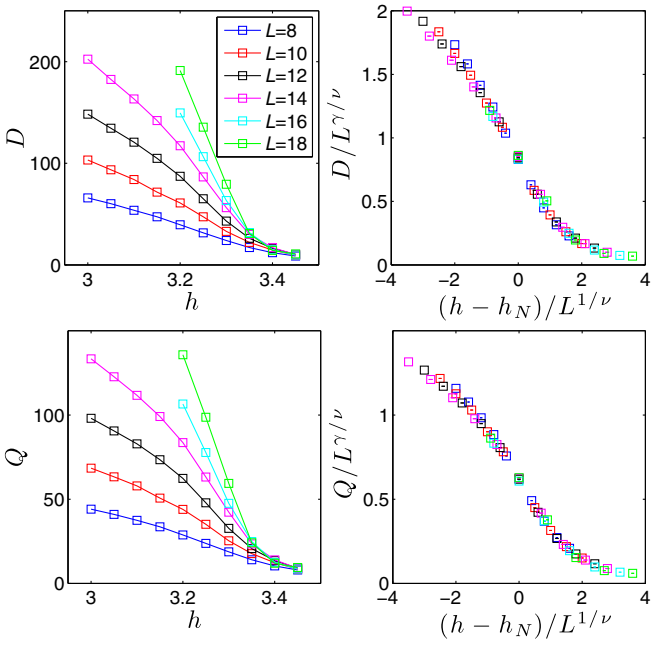

FIG. 20. An example of the procedure used to calculate the critical value of h for a given temperature. Here, for $T = 0.33$, the best data collapse is obtained for $h_N \approx 3.25$. The exponents take the two-dimensional Ising values $\gamma = 7/4$, $\nu = 1$ for this thermal transition. The nematic susceptibility and quadrupolar susceptibility have similar behavior.

APPENDIX C: CHARACTERIZING THE METALLIC STATE

We write the imaginary-time Green function in a spectral representation:

$$G(\mathbf{k},\tau>0) = \langle c_{\mathbf{k}}(\tau)c_{\mathbf{k}}^{\dagger}(0)\rangle = \sum_{m,n}\frac{e^{-\beta\varepsilon_n}}{\Xi}e^{\tau(\varepsilon_n-\varepsilon_m)}|\langle n|c_{\mathbf{k}}|m\rangle|^2. \quad \text{(C1)}$$

Here, $|n\rangle$ is a many-body eigenstate with energy ε_n, and Ξ is the grand partition function. In this representation, the fermion spectral function is

$$A(\mathbf{k},\omega) = \sum_{m,n}\frac{e^{-\beta\varepsilon_n}+e^{-\beta\varepsilon_m}}{\Xi}|\langle n|c_{\mathbf{k}}|m\rangle|^2\delta(\omega+\varepsilon_n-\varepsilon_m), \quad \text{(C2)}$$

and we can write Eq. (C1) as [79]

$$G(\mathbf{k},\tau>0) = \int_{-\infty}^{\infty}d\omega\frac{e^{-\omega(\tau-\beta/2)}}{2\cosh(\beta\omega/2)}A(\mathbf{k},\omega). \quad \text{(C3)}$$

If the ground state is a Fermi liquid, we can extract the quasiparticle weight and Fermi velocity renormalization from Eq. (C3). We assume that at low temperatures, the spectral function in the vicinity of the Fermi surface obtains a Fermi-liquid form, $A(\mathbf{k},\omega) = A_{\rm qp}(\mathbf{k},\omega) + A_{\rm reg}(\mathbf{k},\omega)$, where $A_{\rm qp}$ is the quasiparticle contribution and $A_{\rm reg}(\mathbf{k},\omega)$ is a regular background. In the limit $T\to 0$, $A_{\rm qp}$ becomes a delta-function-like peak: $A_{\rm qp} \approx Z_{\mathbf{k}_F}\delta(\omega-\varepsilon_{\mathbf{k}})$, where $\varepsilon_{\mathbf{k}} = \mathbf{v}_F\cdot(\mathbf{k}-\mathbf{k}_F)$ is the quasiparticle dispersion near the Fermi surface, $Z_{\mathbf{k}_F}$ is the quasiparticle weight, and $\mathbf{v}_F$ is the Fermi velocity. At finite but small T and $\varepsilon_{\mathbf{k}}$, the quasiparticle peak at $\mathbf{k}_F$ obtains a width that scales as $\max(T^2,\varepsilon_{\mathbf{k}}^2)$. The regular part satisfies $A_{\rm reg}(\mathbf{k},\omega) = O[\max(T^2,\omega^2,\varepsilon_{\mathbf{k}}^2)]$.

Inserting the Fermi-liquid form of $A(\mathbf{k},\omega)$ into Eq. (C3), we obtain that at low temperatures,

$$G(\mathbf{k},\tau>0) \approx \frac{Z_{\mathbf{k}_F}e^{-\varepsilon_{\mathbf{k}}(\tau-\beta/2)}}{2\cosh(\beta\varepsilon_{\mathbf{k}}/2)}. \quad \text{(C4)}$$

We can use this relation to estimate $Z_{\mathbf{k}_F}$ and $v_{\mathbf{k}_F}$ along the Fermi surface. For a point on the Fermi surface, $Z_{\mathbf{k}_F} = 2G[\mathbf{k}_F,(\beta/2)]$. The dispersion can be estimated from $\varepsilon_{\mathbf{k}} = -d\log[G(\mathbf{k},\tau)]/d\tau|_{\tau=\beta/2}$, and the Fermi velocity is then evaluated according to $v_{\mathbf{k}} = \nabla_{\mathbf{k}}\varepsilon_{\mathbf{k}}$. Some caution is needed because, in our finite-size systems, the values of $\mathbf{k}$ are quantized and the $\mathbf{k}$ grid does not, in general, intersect the Fermi surface. One can instead

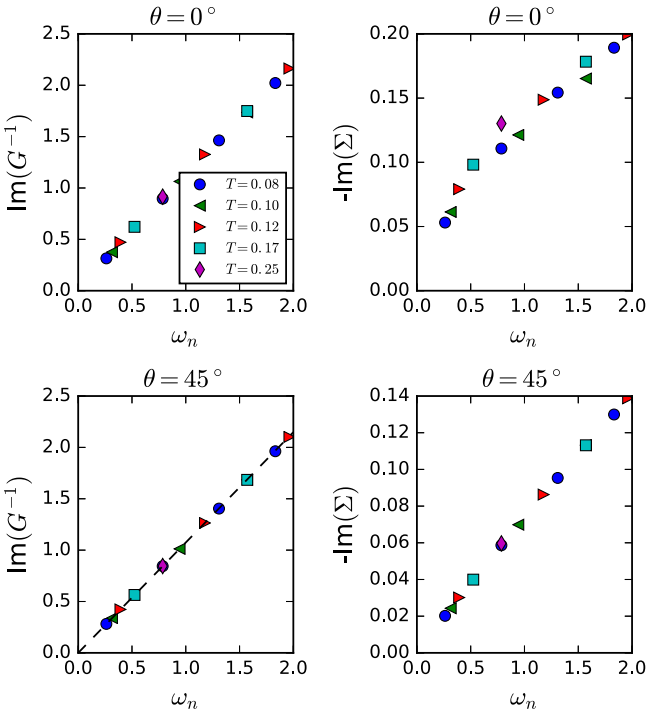

FIG. 21. Left-hand panels: The imaginary part of the inverse of the Matsubara Green function $\mathrm{Im}[G^{-1}(\mathbf{k}_F,\omega_n)]$ for $h = 3.525$. Data points from different temperatures mostly lie on the same curve. Right-hand panels: The imaginary part of the self-energy. The dashed line in the bottom left-hand panel corresponds to $Z = 0.93$.

estimate $Z_{\mathbf{k}}$ from the points nearest to the Fermi surface. Also, our measurements of $G(\mathbf{k},\tau)$ are taken at finite temperatures, yielding the finite-temperature estimators $\tilde{N}(T)$, $\mathbf{v_F}(T)$, and $Z_{\mathbf{k_F}}(T)$ discussed in the text [Eqs. (13), (14), (15)]. An extrapolation to the limit $T \to 0$ is necessary in order to deduce the "true" Fermi-liquid properties, to the extent they are well defined.

APPENDIX D: FERMION GREEN'S FUNCTION AND SELF-ENERGY

In Fig. 21, we show the Matsubara frequency dependence of the inverse fermion Green function. Linear frequency dependence, consistent with a Fermi liquid, seems to dominate down to the lowest frequencies available. Finer details are visible by considering the self-energy (right-hand panels), which shows both a noticeable temperature dependence and a deviation from linearity for $\theta = 0°$.

APPENDIX E: ADDITIONAL DATA

Figure 11 shows the momentum dependence of D^{-1} and Q^{-1} at $h \approx h_c$ and temperatures $T \geq 0.1t$. The momentum dependence at low temperatures is shown in Fig. 22, here plotted versus $|\mathbf{q}|$ instead of $|\mathbf{q}|^2$. Whereas D^{-1} is quadratic in $|\mathbf{q}|$, Q^{-1} is apparently linear in $|\mathbf{q}|$ at low temperatures over a substantial range of momenta, a finding we have not yet understood.

Figures 12 and 14 show D^{-1} and Q^{-1} versus frequency for a variety of momenta, at low temperature and $h \approx h_c$. Figure 23 shows similar data for $h \approx 1.3h_c$, illustrating that deviation from criticality appears mostly through an additive shift of the inverse correlator.

Figure 8 shows the validity of the functional approximant $\mathcal{A}$ of Eq. (6) in describing thermodynamic nematic correlations $D(h,T,\mathbf{q},\omega_n = 0)$. Figure 24 plots D^{-1} versus $\mathcal{A}$ for all frequencies. The agreement is very good except for the smallest momenta, shown in blue and black.

Figure 13 shows the position dependence of the equal time nematic correlator $\tilde{D}$. The analogous data for the equal time quadrupolar correlator $\tilde{Q}$ are somewhat messier. This can be seen in Fig. 25, where we plot the dependence of $\tilde{Q}$

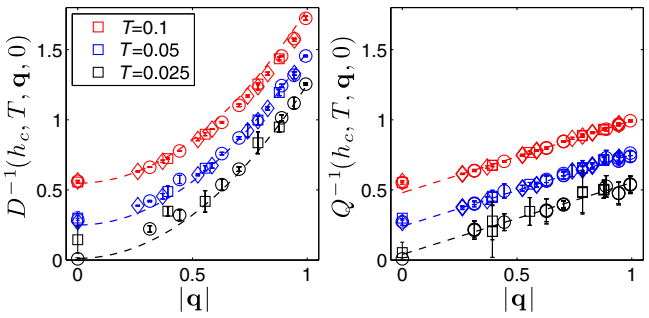

FIG. 22. Inverse nematic and quadrupolar correlators versus $|\mathbf{q}|$ for all orientations of $\mathbf{q}$ at $h = h_c$ and temperatures $T = 0.1, 0.05, 0.025$ (curves are offset for clarity). Momenta from multiple system sizes (represented by squares for $L = 16$, circles for $L = 20$, and diamonds for $L = 24$) fall on the same curve, indicating that the properties shown are in the thermodynamic limit. On the plot of D^{-1} at the left, the dotted lines are the functional approximant, Eq. (6). On the plot of Q^{-1} at the right, the dotted lines are a linear fit to the data at nonzero momentum, with a temperature-independent slope. The apparent linear momentum dependence of Q^{-1} suggests a critical power law, though with an apparently different exponent than the one found in D^{-1}.

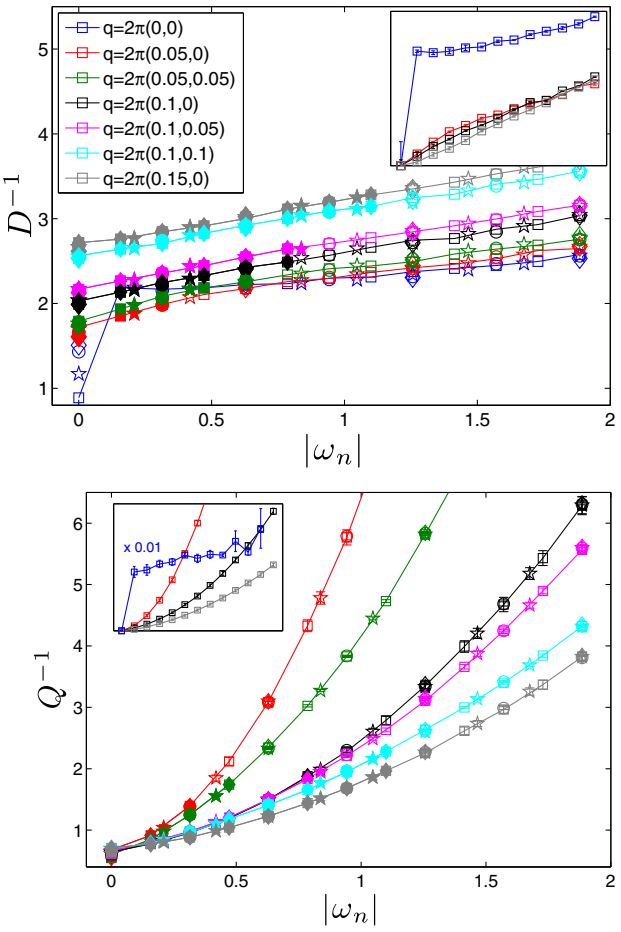

FIG. 23. Frequency dependence of the inverse nematic correlator D^{-1} (top) and inverse quadrupolar correlator Q^{-a} (bottom) at $h = 4.5 \approx 1.3h_c$ for a variety of small momenta $\mathbf{q}$ in an $L = 20$ system at temperatures $T = 0.025$, 0.033, 0.05, 0.1 (shown as squares, stars, circles, and diamonds, respectively). Here, there is a nonvanishing energy scale associated with nematic fluctuations since we are deep in the disordered phase, but the frequency dependence is similar to that at $h = h_c$ (see Fig. 12). Different colors represent different values of $\mathbf{q}$, and filled symbols mark frequencies $|\omega_n| < v_F|\mathbf{q}|$. The insets show the subset of the data with $T = 0.025$ and momenta along the (10) direction shifted by their zero-frequency values. For the inset of the bottom panel, the data at $\mathbf{q} = 0$ are scaled down by a factor of 0.01.

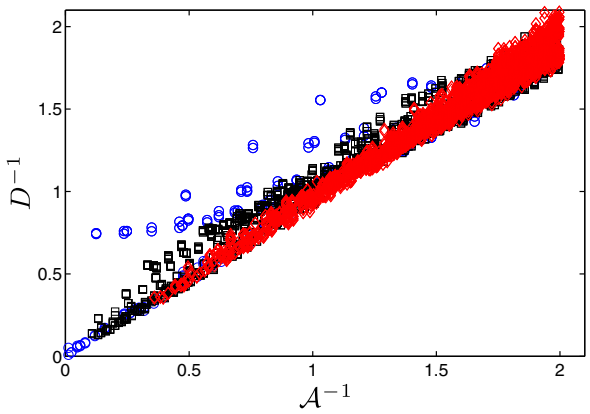

FIG. 24. Comparison between the inverse of the full dynamical functional approximant from Eq. (6), $\mathcal{A}^{-1}$, and the inverse of the nematic correlator D^{-1}. Data shown represent $L = 16$, 20, and 24, $h = 3.525$, 3.7, 3.9, and 4.1, and temperatures $T = 1.0$, 0.67, 0.5, 0.33, 0.25, 0.17, 0.13, 0.1, 0.05, and 0.025. To exhibit the momentum dependence, we use blue circles for $\mathbf{q} = \mathbf{0}$ (403 data points), black squares for $|\mathbf{q}| = (2\pi/L)$ and $(2\pi/L)\sqrt{2}$ (2,840 data points), and red diamonds for all other $\mathbf{q}$ (5,332 data points).

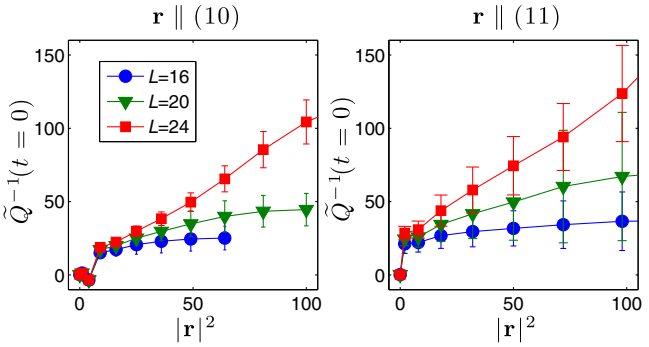

FIG. 25. The inverse of the equal time quadrupolar correlator at $h = h_c$ and $T = 0.1$, plotted versus the square of the spatial separation $\mathbf{r}$ along high-symmetry directions for several system sizes. In contrast to the data of Fig. 13, substantial tetragonal anisotropy can be seen by comparing the left-hand panel (horizontal displacements) and the right-hand panel (diagonal displacements). However, the data apparently represent the thermodynamic limit only for $|\mathbf{r}| \lesssim 4$, and therefore we cannot reliably extract long-distance behavior.

on $\mathbf{r}$ for $\mathbf{r}$ along the symmetry directions (1,0) and (11); as is apparent, the error bars (associated with the sensitivity of the results to boundary conditions) are sufficiently large that it is difficult to conclude much from this figure.

[1] E. Fradkin and S. A. Kivelson, *High-Temperature Superconductivity: Ineluctable Complexity*, Nat. Phys. **8**, 864 (2012).

[2] J. A. Hertz, *Quantum Critical Phenomena*, Phys. Rev. B **14**, 1165 (1976).

[3] A. J. Millis, *Effect of a Nonzero Temperature on Quantum Critical Points in Itinerant Fermion Systems*, Phys. Rev. B **48**, 7183 (1993).

[4] R. B. Laughlin, G. G. Lonzarich, P. Monthoux, and D. Pines, *The Quantum Criticality Conundrum*, Adv. Phys. **50**, 361 (2001).

[5] P. Gegenwart, Q. Si, and F. Steglich, *Quantum Criticality in Heavy-Fermion Metals*, Nat. Phys. **4**, 186 (2008).

[6] A. Rost, S. Grigera, J. Bruin, R. Perry, D. Tian, S. Raghu, S. A. Kivelson, and A. Mackenzie, *Thermodynamics of Phase Formation in the Quantum Critical Metal* $Sr_3Ru_2O_7$, Proc. Natl. Acad. Sci. U.S.A. **108**, 16549 (2011).

[7] A. J. Millis, A. J. Schofield, G. G. Lonzarich, and S. A. Grigera, *Metamagnetic Quantum Criticality*, Phys. Rev. Lett. **88**, 217204 (2002).

[8] Selected recent developments regarding quantum critical behavior in these material families include Refs. [9,10] in cuprates and Refs. [11,12] in Fe-based superconductors.

[9] B. J. Ramshaw, S. E. Sebastian, R. D. McDonald, J. Day, B. S. Tan, Z. Zhu, J. B. Betts, R. Liang, D. A. Bonn, W. N. Hardy, and N. Harrison, *Quasiparticle Mass Enhancement Approaching Optimal Doping in a High-T_c Superconductor*, Science **348**, 317 (2015).

[10] K. Fujita, C. K. Kim, I. Lee, J. Lee, M. H. Hamidian, I. A. Firmo, S. Mukhopadhyay, H. Eisaki, S. Uchida, M. J. Lawler, E.-A. Kim, and J. C. Davis, *Simultaneous Transitions in Cuprate Momentum-Space Topology and Electronic Symmetry Breaking*, Science **344**, 612 (2014).

[11] H.-H. Kuo, J.-H. Chu, S. A. Kivelson, and I. R. Fisher, *Ubiquitous Signatures of Nematic Quantum Criticality in Optimally Doped Fe-Based Superconductors*, Science **352**, 958 (2016).

[12] K. Hashimoto, K. Cho, T. Shibauchi, S. Kasahara, Y. Mizukami, R. Katsumata, Y. Tsuruhara, T. Terashima, H. Ikeda, M. Tanatar *et al.*, *A Sharp Peak of the Zero-Temperature Penetration Depth at Optimal Composition in* $BaFe_2(As_{1-x}P_x)_2$, Science **336**, 1554 (2012).

[13] P. A. Lee, *Gauge Field, Aharonov-Bohm Flux, and High-T_c Superconductivity*, Phys. Rev. Lett. **63**, 680 (1989).

[14] C. Castellani, C. Di Castro, and M. Grilli, *Non-Fermi-Liquid Behavior and d-Wave Superconductivity near the Charge-Density-Wave Quantum Critical Point*, Z. Phys. B **103**, 137 (1996).

[15] C. M. Varma, *Non-Fermi-Liquid States and Pairing Instability of a General Model of Copper Oxide Metals*, Phys. Rev. B **55**, 14554 (1997).

[16] A. Rosch, *Interplay of Disorder and Spin Fluctuations in the Resistivity near a Quantum Critical Point*, Phys. Rev. Lett. **82**, 4280 (1999).

[17] L. Dell'Anna and W. Metzner, *Electrical Resistivity near Pomeranchuk Instability in Two Dimensions*, Phys. Rev. Lett. **98**, 136402 (2007).

[18] D. L. Maslov, V. I. Yudson, and A. V. Chubukov, *Resistivity of a Non-Galilean–Invariant Fermi Liquid near Pomeranchuk Quantum Criticality*, Phys. Rev. Lett. **106**, 106403 (2011).

[19] V. Barzykin and D. Pines, *Phenomenological Model of Protected Behavior in the Pseudogap State of Underdoped Cuprate Superconductors*, Phys. Rev. Lett. **96**, 247002 (2006).

[20] S. A. Hartnoll, R. Mahajan, M. Punk, and S. Sachdev, *Transport near the Ising-Nematic Quantum Critical Point of Metals in Two Dimensions*, Phys. Rev. B **89**, 155130 (2014).
[21] B. L. Altshuler, L. B. Ioffe, and A. J. Millis, *Low-Energy Properties of Fermions with Singular Interactions*, Phys. Rev. B **50**, 14048 (1994).
[22] C. Nayak and F. Wilczek, *Renormalization Group Approach to Low Temperature Properties of a Non-Fermi Liquid Metal*, Nucl. Phys. **B430**, 534 (1994).
[23] C. Nayak and F. Wilczek, *Non-Fermi Liquid Fixed Point in* $2+1$ *Dimensions*, Nucl. Phys. **B417**, 359 (1994).
[24] B. L. Altshuler, L. B. Ioffe, and A. J. Millis, *Critical Behavior of the* $T=0$ $2k_F$ *Density-Wave Phase Transition in a Two-Dimensional Fermi Liquid*, Phys. Rev. B **52**, 5563 (1995).
[25] A. Abanov and A. V. Chubukov, *A Relation between the Resonance Neutron Peak and ARPES Data in Cuprates*, Phys. Rev. Lett. **83**, 1652 (1999).
[26] A. Abanov and A. V. Chubukov, *Spin-Fermion Model near the Quantum Critical Point: One-Loop Renormalization Group Results*, Phys. Rev. Lett. **84**, 5608 (2000).
[27] A. Abanov, A. Chubukov, and J. Schmalian, *Quantum-Critical Theory of the Spin-Fermion Model and Its Application to Cuprates: Normal State Analysis*, Adv. Phys. **52**, 119 (2003).
[28] A. Abanov and A. Chubukov, *Anomalous Scaling at the Quantum Critical Point in Itinerant Antiferromagnets*, Phys. Rev. Lett. **93**, 255702 (2004).
[29] M. J. Lawler, D. G. Barci, V. Fernández, E. Fradkin, and L. Oxman, *Nonperturbative Behavior of the Quantum Phase Transition to a Nematic Fermi Fluid*, Phys. Rev. B **73**, 085101 (2006).
[30] H. v. Löhneysen, A. Rosch, M. Vojta, and P. Wölfle, *Fermi-Liquid Instabilities at Magnetic Quantum Phase Transitions*, Rev. Mod. Phys. **79**, 1015 (2007).
[31] S.-S. Lee, *Low-Energy Effective Theory of Fermi Surface Coupled with U(1) Gauge Field in* $2+1$ *Dimensions*, Phys. Rev. B **80**, 165102 (2009).
[32] M A. Metlitski and S. Sachdev, *Quantum Phase Transitions of Metals in Two Spatial Dimensions. I. Ising-Nematic Order*, Phys. Rev. B **82**, 075127 (2010).
[33] M. A. Metlitski and S. Sachdev, *Quantum Phase Transitions of Metals in Two Spatial Dimensions. II. Spin Density Wave Order*, Phys. Rev. B **82**, 075128 (2010).
[34] D. F. Mross, J. McGreevy, H. Liu, and T. Senthil, *Controlled Expansion for Certain Non-Fermi-Liquid Metals*, Phys. Rev. B **82**, 045121 (2010).
[35] D. L. Maslov and A. V. Chubukov, *Fermi Liquid near Pomeranchuk Quantum Criticality*, Phys. Rev. B **81**, 045110 (2010).
[36] P. Wölfle and E. Abrahams, *Quasiparticles beyond the Fermi Liquid and Heavy Fermion Criticality*, Phys. Rev. B **84**, 041101 (2011).
[37] A. L. Fitzpatrick, S. Kachru, J. Kaplan, and S. Raghu, *Non-Fermi-Liquid Fixed Point in a Wilsonian Theory of Quantum Critical Metals*, Phys. Rev. B **88**, 125116 (2013).
[38] D. Dalidovich and S.-S. Lee, *Perturbative Non-Fermi Liquids from Dimensional Regularization*, Phys. Rev. B **88**, 245106 (2013).
[39] T. Holder and W. Metzner, *Anomalous Dynamical Scaling from Nematic and U(1) Gauge Field Fluctuations in Two-Dimensional Metals*, Phys. Rev. B **92**, 041112 (2015).
[40] A. J. Millis, *Nearly Antiferromagnetic Fermi Liquids: An Analytic Eliashberg Approach*, Phys. Rev. B **45**, 13047 (1992).
[41] A. Abanov, A. V. Chubukov, and A. M. Finkel'stein, *Coherent vs. Incoherent Pairing in 2D Systems near Magnetic Instability*, Europhys. Lett. **54**, 488 (2001).
[42] R. Roussev and A. J. Millis, *Quantum Critical Effects on Transition Temperature of Magnetically Mediated p-Wave Superconductivity*, Phys. Rev. B **63**, 140504 (2001).
[43] M. A. Metlitski and S. Sachdev, *Instabilities near the Onset of Spin Density Wave Order in Metals*, New J. Phys. **12**, 105007 (2010).
[44] Y. Wang and A. V. Chubukov, *Superconductivity at the Onset of Spin-Density-Wave Order in a Metal*, Phys. Rev. Lett. **110**, 127001 (2013).
[45] T. A. Maier and D. J. Scalapino, *Pairing Interaction near a Nematic Quantum Critical Point of a Three-Band* CuO_2 *Model*, Phys. Rev. B **90**, 174510 (2014).
[46] S. Lederer, Y. Schattner, E. Berg, and S. A. Kivelson, *Enhancement of Superconductivity near a Nematic Quantum Critical Point*, Phys. Rev. Lett. **114**, 097001 (2015).
[47] M. A. Metlitski, D. F. Mross, S. Sachdev, and T. Senthil, *Cooper Pairing in Non-Fermi Liquids*, Phys. Rev. B **91**, 115111 (2015).
[48] M. Einenkel, H. Meier, C. Pépin, and K. B. Efetov, *Pairing Gaps near Ferromagnetic Quantum Critical Points*, Phys. Rev. B **91**, 064507 (2015).
[49] K. B. Efetov, H. Meier, and C. Pépin, *Pseudogap State Near a Quantum Critical Point*, Nat. Phys. **9**, 442 (2013).
[50] Y. Wang and A. Chubukov, *Charge-Density-Wave Order with Momentum* $(2Q,0)$ *and* $(0,2Q)$ *within the Spin-Fermion Model: Continuous and Discrete Symmetry Breaking, Preemptive Composite Order, and Relation to Pseudogap in Hole-Doped Cuprates*, Phys. Rev. B **90**, 035149 (2014).
[51] R. Blankenbecler, D. J. Scalapino, and R. L. Sugar, *Monte Carlo Calculations of Coupled Boson-Fermion Systems. I*, Phys. Rev. D **24**, 2278 (1981).
[52] F. F. Assaad, in *Quantum Simulations of Complex Many-Body Systems: From Theory to Algorithms*, Proceedings of Euro Winter School 2002, edited by J. Grotendorst, D. Marx, and A. Muramatsu (John von Neumann Institute for Computing, Julich, 2002), pp. 99–156.
[53] C. Wu and S.-C. Zhang, *Sufficient Condition for Absence of the Sign Problem in the Fermionic Quantum Monte Carlo Algorithm*, Phys. Rev. B **71**, 155115 (2005).
[54] E. Berg, M. A. Metlitski, and S. Sachdev, *Sign-Problem-Free Quantum Monte Carlo of the Onset of Antiferromagnetism in Metals*, Science **338**, 1606 (2012).
[55] Z.-X. Li, Y.-F. Jiang, and H. Yao, *Solving the Fermion Sign Problem in Quantum Monte Carlo Simulations by Majorana Representation*, Phys. Rev. B **91**, 241117 (2015).
[56] F. F. Assaad and I. F. Herbut, *Pinning the Order: The Nature of Quantum Criticality in the Hubbard Model on Honeycomb Lattice*, Phys. Rev. X **3**, 031010 (2013).
[57] Z.-X. Li, Y.-F. Jiang, and H. Yao, *Fermion-Sign-Free Majarana-Quantum-Monte-Carlo Studies of Quantum*

Critical Phenomena of Dirac Fermions in Two Dimensions, New J. Phys. **17**, 085003 (2015).

[58] L. Wang, P. Corboz, and M. Troyer, *Fermionic Quantum Critical Point of Spinless Fermions on a Honeycomb Lattice*, New J. Phys. **16**, 103008 (2014).

[59] X. Y. Xu, K. S. D. Beach, F. F. Assaad, and Z. Y. Meng, *Anisotropic Velocity Fluctuations of Dirac Fermions*, arXiv:1602.07150.

[60] R. A. Borzi, S. A. Grigera, J. Farrell, R. S. Perry, S. J. S. Lister, S. L. Lee, D. A. Tennant, Y. Maeno, and A. P. Mackenzie, *Formation of a Nematic Fluid at High Fields in* $Sr_3Ru_2O_7$, Science **315**, 214 (2007).

[61] V. Hinkov, D. Haug, B. Fauqué, P. Bourges, Y. Sidis, A. Ivanov, C. Bernhard, C. T. Lin, and B. Keimer, *Electronic Liquid Crystal State in Superconducting* $YBa_2Cu_3O_{6.45}$, Science **319**, 597 (2008).

[62] R. Daou, J. Chang, D. LeBoeuf, O. Cyr-Choinière, F. Laliberté, N. Doiron-Leyraud, B. J. Ramshaw, R. Liang, D. A. Bonn, W. N. Hardy, and L. Taillefer, *Broken Rotational Symmetry in the Pseudogap Phase of a High-*T_c *Superconductor*, Nature (London) **463**, 519 (2010).

[63] M. Lawler, K. Fujita, J. Lee, A. Schmidt, Y. Kohsaka, C. K. Kim, H. Eisaki, S. Uchida, J. Davis, J. Sethna *et al.*, *Intra-Unit-Cell Electronic Nematicity of the High-Tc Copper-Oxide Pseudogap States*, Nature (London) **466**, 347 (2010).

[64] C.-L. Song, Y.-L. Wang, P. Cheng, Y.-P. Jiang, W. Li, T. Zhang, Z. Li, K. He, L. Wang, J.-F. Jia *et al.*, *Direct Observation of Nodes and Twofold Symmetry in FeSe Superconductor*, Science **332**, 1410 (2011).

[65] S. C. Riggs, M. C. Shapiro, A. V. Maharaj, S. Raghu, E. D. Bauer, R. E. Baumbach, P. Giraldo-Gallo, M. Wartenbe, and I. R. Fisher, *Evidence for a Nematic Component to the Hidden-Order Parameter in* URu_2Si_2 *from Differential Elastoresistance Measurements*, Nat. Commun. **6**, 6425 (2015).

[66] J.-H. Chu, H.-H. Kuo, J. G. Analytis, and I. R. Fisher, *Divergent Nematic Susceptibility in an Iron Arsenide Superconductor*, Science **337**, 710 (2012).

[67] Y. Gallais, R. M. Fernandes, I. Paul, L. Chauvière, Y.-X. Yang, M.-A. Méasson, M. Cazayous, A. Sacuto, D. Colson, and A. Forget, *Observation of Incipient Charge Nematicity in* $Ba(Fe_{1-x}Co_x)_2As_2$, Phys. Rev. Lett. **111**, 267001 (2013).

[68] R. Zhou, Z. Li, J. Yang, D. Sun, C. Lin, and G.-q. Zheng, *Quantum Criticality in Electron-Doped* $BaFe_{2-x}Ni_xAs_2$, Nat. Commun. **4**, 2265 (2013).

[69] A. E. Böhmer, P. Burger, F. Hardy, T. Wolf, P. Schweiss, R. Fromknecht, M. Reinecker, W. Schranz, and C. Meingast, *Nematic Susceptibility of Hole-Doped and Electron-Doped* $BaFe_2As_2$ *Iron-Based Superconductors from Shear Modulus Measurements*, Phys. Rev. Lett. **112**, 047001 (2014).

[70] V. K. Thorsmølle, M. Khodas, Z. P. Yin, C. Zhang, S. V. Carr, P. Dai, and G. Blumberg, *Critical Charge Fluctuations in Iron Pnictide Superconductors*, Phys. Rev. B **93**, 054515 (2016).

[71] P. Jakubczyk, P. Strack, A. A. Katanin, and W. Metzner, *Renormalization Group for Phases with Broken Discrete Symmetry near Quantum Critical Points*, Phys. Rev. B **77**, 195120 (2008).

[72] J. Bauer, P. Jakubczyk, and W. Metzner, *Critical Temperature and Ginzburg Region near a Quantum Critical Point in Two-Dimensional Metals*, Phys. Rev. B **84**, 075122 (2011).

[73] C. M. Varma, P. B. Littlewood, S. Schmitt-Rink, E. Abrahams, and A. E. Ruckenstein, *Phenomenology of the Normal State of Cu-O High-Temperature Superconductors*, Phys. Rev. Lett. **63**, 1996 (1989).

[74] W. Metzner, D. Rohe, and S. Andergassen, *Soft Fermi Surfaces and Breakdown of Fermi-Liquid Behavior*, Phys. Rev. Lett. **91**, 066402 (2003).

[75] D. J. Scalapino, S. R. White, and S. Zhang, *Insulator, Metal, or Superconductor: The Criteria*, Phys. Rev. B **47**, 7995 (1993).

[76] T. Paiva, R. R. dos Santos, R. T. Scalettar, and P. J. H. Denteneer, *Critical Temperature for the Two-Dimensional Attractive Hubbard Model*, Phys. Rev. B **69**, 184501 (2004).

[77] F. F. Assaad, *Depleted Kondo Lattices: Quantum Monte Carlo and Mean-Field Calculations*, Phys. Rev. B **65**, 115104 (2002).

[78] The paramagnetic sign of the orbital susceptibility is probably a band structure effect. For example, in a non-interacting tight-binding model on a square lattice, the orbital susceptibility is paramagnetic in a range of densities near half filling. Near the band bottom (or top), it becomes diamagnetic.

[79] N. Trivedi and M. Randeria, *Deviations from Fermi-Liquid Behavior above* T_c *in 2D Short Coherence Length Superconductors*, Phys. Rev. Lett. **75**, 312 (1995).

[80] T. Senthil, *Critical Fermi Surfaces and Non-Fermi Liquid Metals*, Phys. Rev. B **78**, 035103 (2008).

[81] T. Holstein, R. E. Norton, and P. Pincus, *de Haas–van Alphen Effect and the Specific Heat of an Electron Gas*, Phys. Rev. B **8**, 2649 (1973).

[82] M. Y. Reizer, *Relativistic Effects in the Electron Density of States, Specific Heat, and the Electron Spectrum of Normal Metals*, Phys. Rev. B **40**, 11571 (1989).

[83] B. I. Halperin, P. A. Lee, and N. Read, *Theory of the Half-Filled Landau Level*, Phys. Rev. B **47**, 7312 (1993).

[84] V. Oganesyan, S. A. Kivelson, and E. Fradkin, *Quantum Theory of a Nematic Fermi Fluid*, Phys. Rev. B **64**, 195109 (2001).

[85] S. Sachdev, *Quantum Phase Transitions* (Wiley Online Library, New York, 2007).

[86] In $d = 0$ as well, the Kondo problem can be mapped [87] to the problem of a two-level system coupled to an Ohmic heat bath, for which the nonlocal effective action is equivalent to that of a $d = 1$ classical inverse-square Ising model. This problem can, in turn, be treated using a suitable RG analysis [88].

[87] S. Chakravarty and A. J. Leggett, *Dynamics of the Two-State System with Ohmic Dissipation*, Phys. Rev. Lett. **52**, 5 (1984).

[88] P. W. Anderson, G. Yuval, and D. Hamann, *Exact Results in the Kondo Problem. II. Scaling Theory, Qualitatively Correct Solution, and Some New Results*

on One-Dimensional Classical Statistical Models, Phys. Rev. B **1**, 4464 (1970).

[89] To our knowledge, the temperature dependence of the quantity $Z(T)$ defined here has not been explicitly computed within the Hertz-Millis approach. Applying ω/T scaling to the $T = 0$ self-energy (which, of course, may not be valid) yields $Z(T) \sim T^{1/3}$, a noticeably more rapid variation than the data of Fig. 18(d).

[90] Though our Fermi surface is large, there is a small spanning vector $Q = (2\pi) \times 0.23$ connecting Fermi surface copies in adjacent Brillouin zones (see Fig. 2), and this might lead to a crossover scale at small momentum.

[91] Preliminary results for stronger values $\alpha \geq 1$ of the coupling constant between the fermions and the critical fluctuations [92] provide further evidence for such a crossover. However, at these stronger couplings we also find an intervening superconducting dome obscuring the QCP, which again makes the interpretation of these results in terms of an asymptotic scaling analysis somewhat problematic.

[92] S. Lederer, Y. Schattner, E. Berg, and S. A. Kivelson (to be published).

[93] S. Chakravarty, R. E. Norton, and O. F. Syljuåsen, *Transverse Gauge Interactions and the Vanquished Fermi Liquid*, Phys. Rev. Lett. **74**, 1423 (1995).

[94] T. Senthil and R. Shankar, *Fermi Surfaces in General Codimension and a New Controlled Nontrivial Fixed Point*, Phys. Rev. Lett. **102**, 046406 (2009).

[95] M. J. Lawler, D. G. Barci, V. Fernández, E. Fradkin, and L. Oxman, *Nonperturbative Behavior of the Quantum Phase Transition to a Nematic Fermi Fluid*, Phys. Rev. B **73**, 085101 (2006).

[96] M. J. Lawler and E. Fradkin, *Local Quantum Criticality in the Nematic Quantum Phase Transition of a Fermi Fluid*, Phys. Rev. B **75**, 033304 (2007).

[97] C. M. Varma, *Pseudogap Phase and the Quantum-Critical Point in Copper-Oxide Metals*, Phys. Rev. Lett. **83**, 3538 (1999).

[98] Q. Si, S. Rabello, K. Ingersent, and J. L. Smith, *Locally Critical Quantum Phase Transitions in Strongly Correlated Metals*, Nature (London) **413**, 804 (2001).

[99] A. L. Fitzpatrick, S. Kachru, J. Kaplan, and S. Raghu, *Non-Fermi-Liquid Behavior of Large-N_B Quantum Critical Metals*, Phys. Rev. B **89**, 165114 (2014).

[100] E. Fradkin, S. A. Kivelson, M. J. Lawler, J. P. Eisenstein, and A. P. MacKenzie, *Nematic Fermi Fluids in Condensed Matter Physics*, Annu. Rev. Condens. Matter Phys. **1**, 153 (2010).

[101] S. A. Kivelson, E. Fradkin, and V. J. Emery, *Electronic Liquid-Crystal Phases of a Doped Mott Insulator*, Nature (London) **393**, 550 (1998).

[102] L. Nie, G. Tarjus, and S. A. Kivelson, *Quenched Disorder and Vestigial Nematicity in the Pseudogap Regime of the Cuprates*, Proc. Natl. Acad. Sci. U.S.A. **111**, 7980 (2014).

[103] C. Fang, H. Yao, W.-F. Tsai, J. P. Hu, and S. A. Kivelson, *Theory of Electron Nematic Order in* LaFeAsO, Phys. Rev. B **77**, 224509 (2008).

[104] C. Xu, M. Müller, and S. Sachdev, *Ising and Spin Orders in the Iron-Based Superconductors*, Phys. Rev. B **78**, 020501 (2008).

[105] M. Punk, *Finite Temperature Scaling Close to Ising-Nematic Quantum Critical Points in Two-Dimensional Metals*, arXiv:1606.00918.

[106] U. Wolff, *Collective Monte Carlo Updating for Spin Systems*, Phys. Rev. Lett. **62**, 361 (1989).